Reviewed Preprint

Published from the original preprint after peer review and assessment by eLife.

About eLife's process

Reviewed preprint posted
5 May 2023 (this version)

Posted to Research Square
13 January 2023

Sent for peer review
11 January 2023

Cell Biology, Neuroscience

RNA-binding deficient TDP-43 drives cognitive decline in a mouse model of TDP-43 proteinopathy

Julie Necarsulmer, Jeremy Simon, Baggio Evangelista, Youjun Chen, Xu Tian, Sara Nafees, Ariana Marquez Gonzalez, Ping Wang, Deepa Ajit, Viktoriya Nikolova, Kathryn Harper, Jennifer Ezzell, Adriana Beltran, Sheryl Moy, Todd Cohen ✉

University of North Carolina at Chapel Hill • UNC Chapel Hill • University of North Carolina

Abstract

TDP-43 proteinopathies including frontotemporal lobar dementia (FTLD) and amyotrophic lateral sclerosis (ALS) are neurodegenerative disorders characterized by aggregation and mislocalization of the nucleic-acid binding protein TDP-43 and subsequent neuronal dysfunction. Here, we developed an endogenous model of sporadic TDP-43 proteinopathy based on the principle that disease-associated TDP-43 acetylation at lysine 145 (K145) alters TDP-43 conformation, impairs RNA-binding capacity, and induces downstream mis-regulation of target genes. Expression of acetylation-mimic TDP-43^{K145Q} resulted in stress-induced nuclear TDP-43 foci and loss-of-TDP-43-function in primary mouse and human induced pluripotent stem cell (hiPSC)-derived cortical neurons. Mice harboring the TDP-43^{K145Q} mutation recapitulated key hallmarks of FTLD, including progressive TDP-43 phosphorylation and insolubility, TDP-43 mis-localization, transcriptomic and splicing alterations, and cognitive dysfunction. Our study supports a model in which TDP-43 acetylation drives neuronal dysfunction and cognitive decline through aberrant splicing and transcription of critical genes that regulate synaptic plasticity and stress response signaling. The neurodegenerative cascade initiated by TDP-43 acetylation recapitulates many aspects of FTLD and provides a new paradigm to further interrogate TDP-43 proteinopathies.

eLife assessment

Necarsulmer et al describe an interesting new mouse model of TDP-43 proteinopathy in which gene editing was used to introduce a K145Q acetylation-mimic mutation previously shown to impair RNA-binding capacity and induce downstream misregulation of target genes. Mice homozygous for this mutation are **convincingly** shown to display cognitive/behavioral impairment, TDP-43 phosphorylation and insolubility, and changes in gene expression and splicing. This novel mouse model replicates some **important** hallmarks of human frontotemporal lobar degeneration and will be an **important** contribution to the field after several points are adequately addressed.

Introduction

TDP-43 proteinopathies are characterized by the dysfunction and aggregation of Transactivation response element DNA-binding Protein of 43 kDa (TDP-43), with ~ 95% of all amyotrophic lateral sclerosis (ALS) and ~ 50-60% of all frontotemporal lobar dementia (FTLD-TDP) cases harboring TDP-43 pathology(1)–(4). There is significant neuropathologic and clinical overlap between FTLD and ALS with many individuals developing a mixed phenotype, providing strong evidence for a common FTLD/ALS spectrum of disorders(5)–(9). It is also notable that TDP-43 pathology is abundant in other sporadic neurodegenerative diseases including Alzheimer disease (AD)(10),(11), Limbic-Predominant Age-related TDP-43 Encephalopathy (LATE)(12),(13), and Parkinson's disease (PD)(14),(15). The clinical and neuropathological overlap suggests that common pathogenic mechanisms may link TDP-43 to neurodegeneration(16),(17). However, modeling sporadic TDP-43 pathogenesis has been challenging since its expression levels are tightly regulated(18),(19), which has precluded a clear separation of TDP-43 disease-related dysfunction from general toxicity resulting from TDP-43 over- or under-expression(20)–(23). Current knock-in models of TDP-43 disease-causing mutations(24)–(28) provide valuable insights but may be limited in their application to sporadic disease.

Under normal physiological conditions, TDP-43 resides in the nucleus to control RNA processing (RNA splicing, transport, and stability) and gene transcription(29)–(31). Structurally, nuclear retention is primarily mediated by an N-terminal nuclear localization sequence (NLS) through interactions with α1/β-importins(32),(33), and association with nucleic acids is mediated by two tandem RNA recognition motifs (RRM1/RRM2)(34),(35) (Fig. S1A), however there is interplay between nucleic acid binding and nuclear localization(36),(37). The C-terminal glycine-rich domain (also termed the intrinsically disordered or low complexity domain) mediates protein-protein interactions(37)–(39) and harbors most, but not all, familial *TARDBP* mutations that are causative for FTLD/ALS(40),(41). In sporadic or familial TDP-43 proteinopathies, TDP-43 undergoes nuclear depletion and concomitant nuclear or cytoplasmic accumulation and aggregation(42)–(44). Both TDP-43 loss-of-function (e.g., aberrant cryptic splicing) and gain-of-function (e.g., aggregate-induced toxicity) mechanisms have been proposed as drivers of TDP-43 pathogenesis(45)–(48).

How TDP-43 becomes dysfunctional in sporadic disease remains unresolved, however TDP-43 post-translational modifications (PTMs) such as phosphorylation, acetylation, and ubiquitination modulate TDP-43's biochemical properties leading to conformational changes, modulation of nucleic acid binding affinity, regulation of liquid-liquid phase separation (LLPS), and propensity to form insoluble TDP-43 aggregates(49)–(51). Among the various PTMs, TDP-43 acetylation at lysine residue 145 (K145) within RRM1 has emerged as a regulator of both loss and gain of function toxicity(52),(53). Acetylated TDP-43 is found within TDP-43 inclusions of sporadic ALS (sALS) spinal cord motor neurons but not age-matched control tissue(52). Inclusions in FTLD cortex are largely composed of C-terminal fragmented TDP-43 lacking the K145 residue(54),(55), precluding an assessment of Ac-K145 in FTLD patients. However, *TARDBP* mutations that disrupt RNA binding, and thereby may act in a similar manner to TDP-43 acetylation, have been identified in FTLD-TDP patients(56)–(58), supporting a pathogenic role of altered nucleic acid binding in disease. Mimicking TDP-43 acetylation with a lysine-to-glutamine substitution (TDP-43^{K145Q}) is sufficient to neutralize the positive charge, disrupt RNA binding, and induce several hallmarks of TDP-43 pathology *in vitro*(52),(53), supporting a model whereby TDP-43 acetylation drives both loss-of-function (e.g., RNA-binding deficiency) and gain-of-function (e.g., aggregation) toxicity.

in mice, which enabled us to investigate the potential pathophysiological impacts of an aberrant TDP-43 PTM without disturbing up- or downstream genomic elements that govern TDP-43 autoregulation. Using mouse cortical neurons, human hiPSC-derived cortical neurons, and aged cohorts of TDP-43^{K145Q} homozygous mice, we found that acetylation-mimic TDP-43^{K145Q} induced nuclear TDP-43 foci and cytoplasmic TDP-43 accumulation, which coincided with several disease-associated and loss-of-function measures including widespread transcriptome and splicing alterations. Finally, we observed prominent FTLD-like cognitive and behavioral deficits in acetylation-mimic TDP-43 mice that correlated with neurodegeneration and TDP-43 biochemical abnormalities in affected brain regions. Our study supports lysine acetylation as a driver of TDP-43 dysfunction and neurodegeneration in sporadic TDP-43 proteinopathies.

Results

Neurons expressing TDP-43^{K145Q} form nuclear TDP-43-positive foci in response to overexpression or oxidative stress

We originally showed that TDP-43 acetylation can promote RNA-binding deficiency, aggregation, and pathology(52),(53). We sought to expand these findings by exploring the behavior of acetylation-mimic TDP-43 variants in primary murine cortical neurons. We employed lentiviral vectors that encode either wild-type (TDP-43^{wt}), acetylation-deficient (TDP-43^{K145R}), and acetylation-mimic (TDP-43^{K145Q}) variants to overexpress TDP-43 species in neurons, and then examined their subcellular localization by immunofluorescence microscopy. In the absence of acute cellular stress, most neurons overexpressing TDP-43^{K145Q} showed distinct nuclear foci that were not detected with TDP-43^{wt} or TDP-43^{K145R} constructs (Fig. 1A, B). When neurons were exposed to acute an oxidative stress (200 µM sodium arsenite), a sensitizing trigger commonly used to enhance TDP-43 dysfunction(59)–(62), there was a significant increase in TDP-43 foci formation with all variants (Fig. 1A, C). The response in neurons expressing TDP-43^{K145Q} was robust, resulting in the formation of numerous large, bright TDP-43-positive foci, as well as small TDP-43-positive nuclear puncta. These aberrant TDP-43 structures, which like represent conformations recently termed anisosomes(63), were absent from cells expressing TDP-43^{wt} or acetylation-null TDP-43^{K145R}, indicating that acetylation-mimic TDP-43^{K145Q} alters TDP-43 conformation within the nucleus, sensitizes neurons to oxidative stress, and drives anisosome formation. By coupling high content wide-field microscopy with quantitative image analysis, we observed a three-fold increase in TDP-43 foci/anisosomes formation in neurons expressing TDP-43^{K145Q} (Fig. 1C).

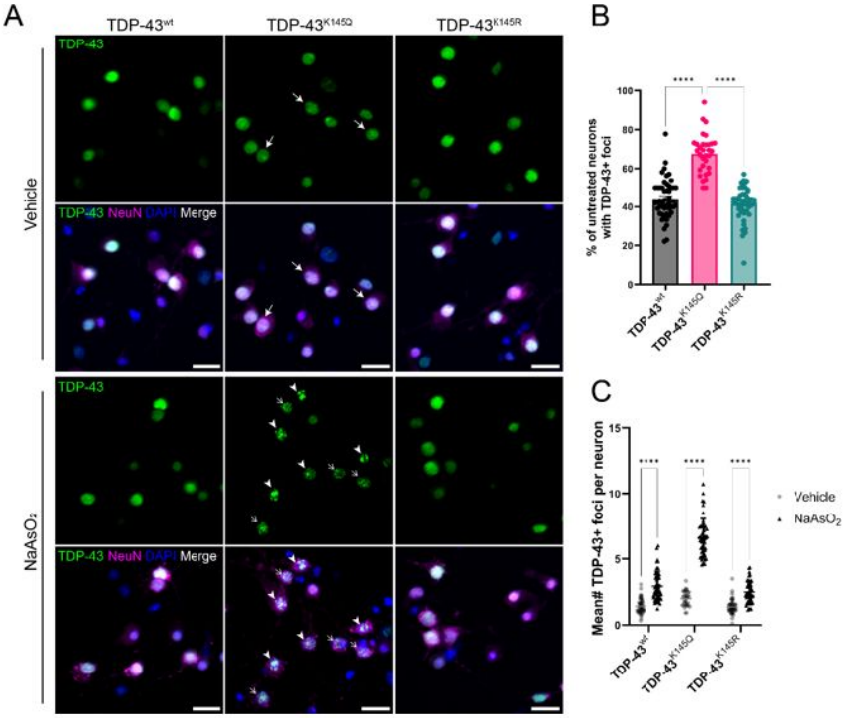

Figure 1

Overexpression of acetylation-mimic TDP-43^{K145Q} enhances TDP-43 stress-induced nuclear foci formation

A Representative images of immunofluorescence evaluation of TDP-43 in DIV14 mouse primary cortical neurons overexpressing TDP-43^{wt}, TDP-43^{K145Q}, or TDP-43^{K145R} after vehicle or 200µM NaAsO^{2} treatment followed by labeling of TDP-43 (green), NeuN (magenta), and DAPI (blue). Stick arrows highlight nuclei with small TDP-43+ puncta and arrowheads highlight nuclei with large TDP-43+ foci. Scale bar = 20µm. **B** Quantification of percentage of neurons with TDP-43+ foci in vehicle-treated neurons [One-way ANOVA followed by Tukey's multiple comparisons testing; main effect of treatment between TDP-43 variants F (3,184) = 66.35, $p<0.0001$]. **C** Quantification of the average number of TDP-43+ foci per neuron [Two-way ANOVA followed by Tukey's multiple comparisons testing; main effect of TDP-43 variant F (3, 343) = 36.23, $p<0.0001$]. Data shown as mean ± SEM. Each data point represents the average value within neurons in a single field of view with 10-100 neurons per field and n=48 fields per condition across 3 biological replicates. Statistical significance is represented by asterisks ****$p<0.0001$. DIV= Day *in vitro*

TDP-43 overexpression can result in general toxicity and altered TDP-43 function, depending on duration and the level of over-expression(20),(64),(65). To avoid potentially confounding non-specific toxicity, we transitioned to a more physiologically relevant model to further elucidate the impact of RNA-binding deficient acetylation-mimic TDP-43. We employed CRISPR-Cas9 mutagenesis to introduce a single amino acid substitution at position 145 (K145Q) in the endogenous mouse *Tardbp* locus, thereby generating the TDP-43^{K145Q} knock-in line (Fig. S1B). By targeting the native mouse gene, we avoid both TDP-43 overexpression and disruption of autoregulatory genomic elements of the endogenous *Tardbp* transcript(18). A TDP-43^{K145Q} founder line was propagated as heterozygotes and continually re-sequenced to confirm retention and propagation of the K145Q substitution (Fig. S1C, D). Both heterozygous and homozygous TDP-43^{K145Q} mice were born at normal mendelian frequencies and showed no obvious developmental defects.

We first investigated the effects of TDP-43^{K145Q} expression in neurons *in vitro* by isolating and culturing primary cortical neurons from homozygous TDP-43^{K145Q}, hereafter referred to as TDP-43$^{KQ/KQ}$ mice and compared them to TDP-43^{wt} -derived neurons. Quantitative image analysis of untreated TDP-43$^{KQ/KQ}$ neurons showed mild nuclear TDP-43 depletion and slightly increased levels of cytoplasmic TDP-43 compared to TDP-43^{wt} (Fig. 2A, C). Exposing neurons to acute oxidative stress induced larger and more abundant TDP-43-positive nuclear foci (anisosomes) in acetylation-mimic TDP-43$^{KQ/KQ}$ neurons than in TDP-

43^{wt} neurons (Fig. 2A, B). Because TDP-43 anisosome formation is associated with loss-of-function defects(63),(66),(67), we next sought to determine if TDP-43 function is impaired. A TDP-43-dependent CFTR splicing reporter was employed, in which a full-length GFP gene is fused to an mCherry gene that is interrupted by exon 9 of CFTR(68). Functional TDP-43 suppresses CFTR exon 9 inclusion(69), thereby promoting expression of both GFP and mCherry, while loss of TDP-43 function allows GFP but not mCherry to be expressed (Fig. 2D) The spliced and unspliced constructs differ greatly in size, facilitating analysis by RT-PCR. A neuron-specific synapsin (hSyn) promoter was used to selectively deliver the CFTR reporter via lentiviral transduction of primary neurons. Using RT-PCR, we observed impaired splicing in TDP-$43^{KQ/KQ}$ neurons, as assessed by reduced exclusion of the CFTR exon 9 (Fig. 2E-F). Overall, these results indicate that a single endogenously expressed acetylation-mimic TDP-43^{K145Q} mutation is sufficient to alter TDP-43 localization, induce TDP-43 phase separation, and impair splicing in a murine primary neuron culture model.

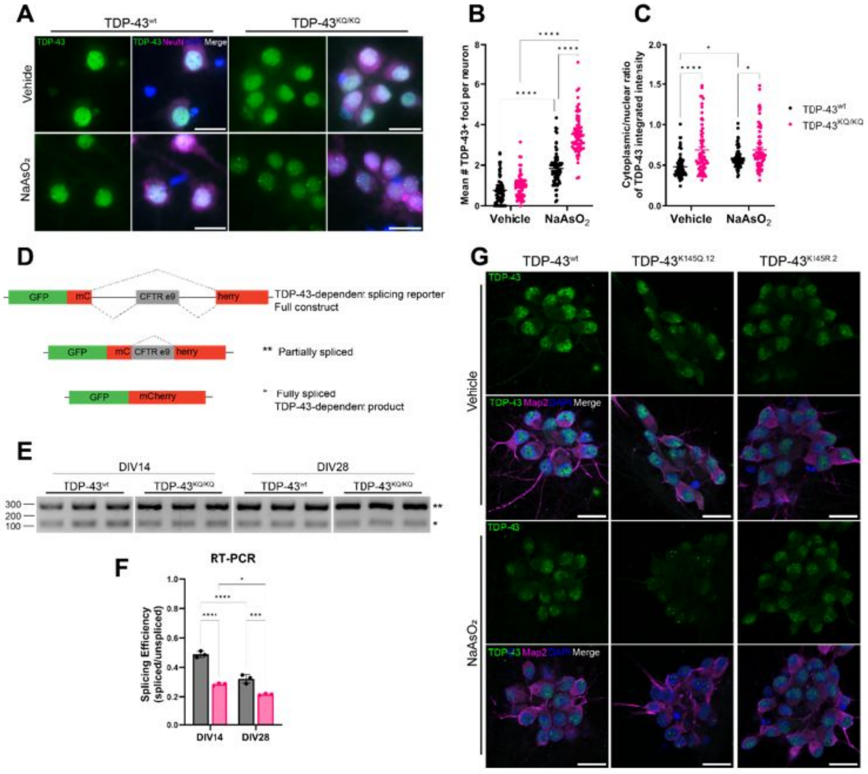

Figure 2

An endogenously encoded acetylation-mimic TDP-43^{K145Q} mutation causes altered TDP-43 localization and functional impairments in mouse and human cortical neurons

A Representative images of primary cortical neurons derived from TDP-43^{wt} or TDP-43$^{KQ/KQ}$ mice that were treated with vehicle or 200μM NaAsO^2 and immunolabeled for endogenous TDP-43 (green), NeuN (magenta), and DAPI (blue). **B-C** Quantification of the number of TDP-43+ neurons and the cytoplasmic:nuclear ratio of TDP-43 fluorescence intensity in TDP-43$^{KQ/KQ}$ compared to TDP-43^{wt} neurons [Data shown as mean ± SEM, with data point representing the average value per neuron in a single field of view, 10-110 neurons per field, n=72 fields across 3 biological replicates; analysis by two-way ANOVA followed by Tukey's multiple comparisons testing; **B** main effect of genotype F (1, 281) = 109.1, $p<0.0001$; **C** main effect of genotype F (1, 274) = 34.05, $p<0.0001$; TDP-43^{wt} vs. TDP-43$^{KQ/KQ}$ +NaAsO^2 p=0.0363; TDP-43^{wt} Vehicle vs +NaAsO^2 p=0.0158]. **D** Schematic of TDP-43 dependent CFTR splicing reporter construct(68),(153). **E** Gel electrophoresis following RT-PCR shows the splicing patterns of CFTR reporter in TDP-43^{wt} and TDP-43$^{KQ/KQ}$ neurons at DIV14 and DIV28. **F** Quantification of band intensity in **e** to yield splicing efficiency values [Data shown as mean ± SD, n=3 biological replicates per condition; analysis by two-way ANOVA followed by Tukey's multiple comparisons testing; main effect of genotype F (1, 8) = 196.6, $p<0.0001$; *p=0.0133]. **G** Representative confocal images of CRISPR-modified human iPSC-derived cortical neurons harboring homozygous TDP-43^{K145Q} (clonal line 12), TDP-43^{K145R} (clonal line 2) knock-in mutations or no *TARDBP* modifications (wt) as a control. Additional clones displayed in Supplementary figure 4. Differentiated cortical neurons were treated with vehicle or 200μM NaAsO^2 and then immunolabeled for endogenous TDP-43 (green), Map2 (magenta), and DAPI (blue). Scale bars = 20μm. Statistical significance is represented by asterisks *$p<0.05$, ***$p<0.001$, ****$p<0.0001$. DIV= *Day in vitro*

To assess this model's relevance to human neurons, we used CRISPR/Cas9 to generate a panel of human induced pluripotent stem cell (hiPSC) lines harboring acetylation-mimic TDP-43 (TDP-43$^{K145Q.12}$ and TDP-43$^{K145Q.18}$), acetylation-deficient TDP-43 (TDP-43$^{K145R.2}$ and TDP-43$^{K145R.12}$), or unmodified TDP-43 (TDP-43^{wt}) (Fig. S2) and differentiated these lines into cortical neurons (Fig. S3). Untreated hiPSC-derived TDP-43^{K145Q} cortical neurons were morphologically identical to TDP-43^{wt} and TDP-43^{K145R} neurons and showed similar patterns of TDP-43 localization (Fig. 2G, Fig. S4). All hiPSC-derived lines showed a granular nuclear TDP-43 localization pattern under normal conditions, consistent with physiologic demixing of nuclear TDP-43(61). Following acute oxidative stress, TDP-43^{K145Q} neurons showed TDP-43 nuclear clearing and the formation of large, intensely labeled TDP-43-positive anisosomes (Fig. 2G, Fig. S4). In comparison, cortical neurons expressing TDP-43^{wt} or TDP-

43^{K145R} maintained nuclear TDP-43 and formed small stippled TDP-43 foci. We note that TDP-43 nuclear clearing and foci formation was more robust in hiPSC-derived neurons compared to mouse neurons, suggesting human neurons may be more sensitive to the effects of RNA-binding deficient TDP-43. Similar to mouse neurons, hiPSC-derived TDP-43^{K145R} neurons were indistinguishable from TDP-43^{wt} neurons, further supporting charge neutralization as a critical driver of TDP-43 loss of function rather than an inherent effect of mutation at the K145 locus.

TDP-43 acetylation-mimic mice develop age-dependent cognitive and behavioral defects

To evaluate neurodegenerative phenotypes in TDP-43 acetylation-mimic mice, we aged homozygous TDP-$43^{KQ/KQ}$ mice and WT littermates and performed an extensive battery of behavioral analysis to assess cognitive and motor function, which reflect impairments that are commonly impacted in the spectrum of TDP-43 proteinopathies(6). Since there were no significant differences between males and females in any behavioral analyses described below, we pooled both sexes into either WT or TDP-$43^{KQ/KQ}$ groups. At 12 months old, TDP-$43^{KQ/KQ}$ mice showed significant reduction of body weight compared to WT littermates, and this difference was maintained until end point analysis at 18 months old (Fig. 3A). Evaluation of exploratory activity and locomotion in an open field test demonstrated that TDP-$43^{KQ/KQ}$ mice spend significantly more time in the center region (Fig. 3B), with no differences in total distance traveled (Fig. S5A), indicative of decreased anxiety-like behavior(70),(71). Acoustic startle testing revealed impaired prepulse inhibition (PPI) at 12 months old (Fig. S6A), indicative of deficits in sensorimotor gating, a form of inhibitory behavioral control, in TDP-$43^{KQ/KQ}$ mice(72),(73), a phenomenon that can be observed in early dementia(74). In 18-month-old animals, evaluation of acoustic startle response and PPI was confounded by hearing impairment (Fig. S6B), however the altered activity reflected by increased time in the center region of an open field test was maintained at this advanced age (Fig. 3B). Thus, consistent patterns of behavioral disinhibition and reduced anxiety-like behavior were apparent in TDP-$43^{KQ/KQ}$ mice over time.

We next performed contextual and cue-dependent fear conditioning as an index of hippocampal and cortical function(75)–(79). Context-dependent fear testing revealed reduced freezing times in TDP-$43^{KQ/KQ}$ mice, with trends observed at 12 months old and more significant deficits at 18 months, suggesting age-dependent impairments in contextual learning (Fig. 3C). Similarly, auditory cue-dependent fear testing revealed significant impairments in associative cue learning in TDP-$43^{KQ/KQ}$ mice at 12 months of age (Fig. 3D), a behavior thought to be mediated by the amygdala and higher-order cortical regions important in inhibitory control(80). As mentioned above, general auditory defects in both genotypes at 18 months of age confounded interpretations of any cue-dependent learning deficits at this advanced age (Fig. 3D).

Morris Water Maze testing was used to evaluate swimming ability and spatial learning(81), which showed equivalent swim speeds, suggesting no motor impairments in TDP-$43^{KQ/KQ}$ mice at 18 months of age (Fig. S5D). While assessment of spatial learning showed a trend towards impaired acquisition learning (Fig. 3E, F), we observed more prominent defects in reversal learning after moving the location of the platform, as determined by significant delays in escape latency. These findings support deficits in cognitive flexibility in TDP-$43^{KQ/KQ}$ mice compared to WT littermates (Fig. 3G, H)(82).

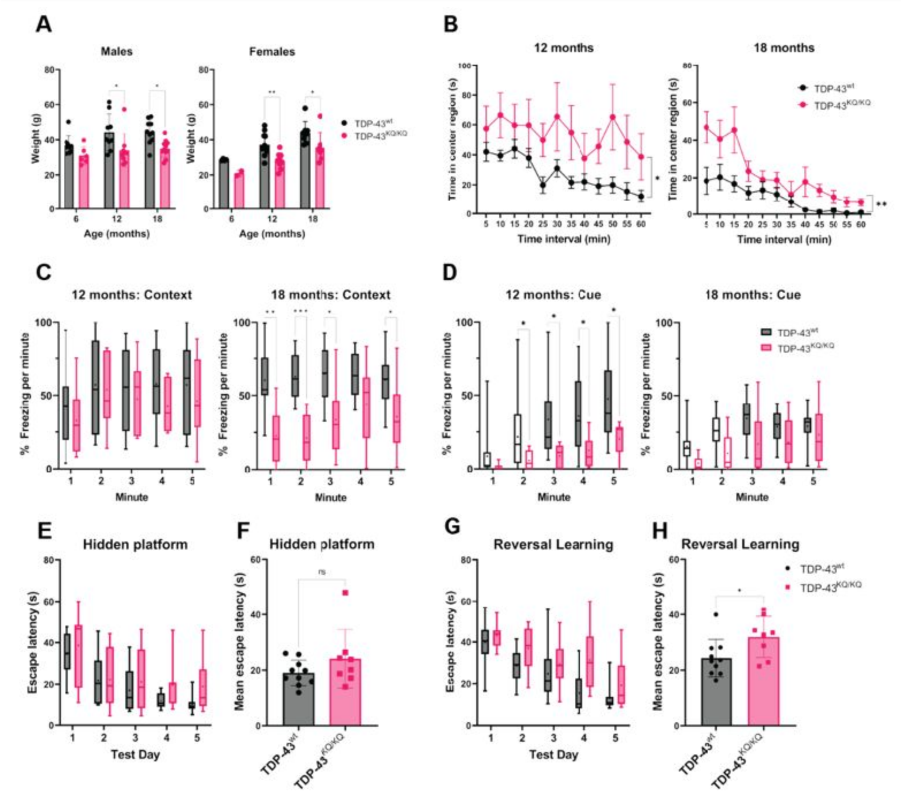

Figure 3

TDP-43$^{KQ/KQ}$ mice develop age-dependent cognitive and behavioral defects.

A Body weight of TDP-43^{wt} and TDP-43$^{KQ/KQ}$ mice in males [left panel; F(1,48)=17.52, p=0.0001] and females [right panel; F(1,36)=14.17, p=0.0006] at different ages. **B** Quantification of time in the center region of an open field in mice at 12 months [left panel; F(1,20)=6.118, p=0.0225] and 18 months [right panel; F(1,17)=9.622, p=0.0065]. **C** Quantification of time spent frozen (immobile) following context-dependent conditioned fear testing 18-months-old [right panel; F(1,17)=5.402, p=0.0328]. **D** Quantification of time spent frozen following cue-dependent conditioned fear testing at 12-months-old [left panel; F(1,20)=5.285, p=0.0324] and 18-months-old. Filled bars represent presence of auditory cue (tone). **E-F** Morris Water Maze (MWM) analysis displaying time to find a hidden platform (escape latency), quantified as daily trial means per animal (**E**) or average across all days (**F**). **G-H** Quantification of escape latencies during MWM reversal learning trials in daily trials (**G**) [F(1,16)=5.273, p=0.0355] and comparing averages per mouse across all days (**H**).

Bar and scatter plots shown as mean ± SD. Box and whiskers show line at median, '+' at mean, and whiskers run min to max. **a** Two-way ANOVA followed by Šídák's multiple comparisons test. **B-D,E,G** Two-way repeated measures ANOVA followed by Holm-Šídák's multiple comparisons tests; **F** statistics and p-values in legend represent main effect of genotype. **F, H** Unpaired student's t-test. Sample sizes as follows unless otherwise indicated: 12-month TDP-43^{wt} n=15; 12-month TDP-43$^{KQ/KQ}$ n=7; 18-month TDP-43^{wt} n=10; 18-month TDP-43$^{KQ/KQ}$ n=9; one 18-month TDP-43$^{KQ/KQ}$ extreme outlier removed for MWM analysis (**E,F**). Statistical significance is represented by asterisks *p<0.05, **p<0.01, ***p<0.001; ns=not significant. Further statistical information is located Figure 3 Source Data 1 file.

Finally, we assessed motor function in these cohorts and were surprised to find no overt signs of motor impairment in TDP-43$^{KQ/KQ}$ mice 18 months of age. TDP-43$^{KQ/KQ}$ mice do not differ from WT littermates in motor coordination as assessed by rotarod testing (Fig. S5C-D) or in grip strength as measured using digital force meters (Fig. S5E). Moreover, there were no differences in swim speed or distance traveled in an open field at any age tested (Fig. S5A, B). The preferential deficits in learning and behavioral control support a prominent FTLD- or dementia-like phenotype in TDP-43$^{KQ/KQ}$ at the ages tested. We note that we cannot currently exclude the possibility of more subtle motor phenotypes or the emergence of motor defects in aged mice beyond 18 months old, which will require follow-up studies.

TDP-43$^{KQ/KQ}$ mice demonstrate TDP-43 dysfunction and neuron loss in neocortex and hippocampus

Given the robust cognitive phenotype observed in TDP-43$^{KQ/KQ}$ mice, which was most pronounced at 18 months, we focused the remainder of this study on the neocortex and hippocampus of aged animals. We first characterized aspects of TDP-43 pathology including TDP-43 aggregation, mislocalization, and neuronal loss(17),(43). To do so, we performed immunohistochemical and immunofluorescent labelling, confocal microscopy, and automated quantitative image analysis to assess TDP-43 localization in 18-month-old TDP-43$^{KQ/KQ}$. Quantification of NeuN-positive cells revealed significantly reduced neuron density in TDP-43$^{KQ/KQ}$ neocortex compared to WT mice (Fig. 4A, B). In contrast, using a Cresyl Violet stain, which labels the rough endoplasmic reticulum and nuclei of all cell types including glia(83), we did not observe significant differences in overall cell density in the neocortex (Fig. 4C, D), suggesting preferential neuronal loss in TDP-43$^{KQ/KQ}$ cortex. Intriguingly, we observed no significant astrogliosis, as measured by intensity and area of GFAP fluorescence, or microgliosis, as measured by intensity and area of Iba1 fluorescence intensity, in the neocortex or hippocampus in 18-month-old TDP-43$^{KQ/KQ}$ mice compared to TDP-43^{wt} animals (Fig. S7).

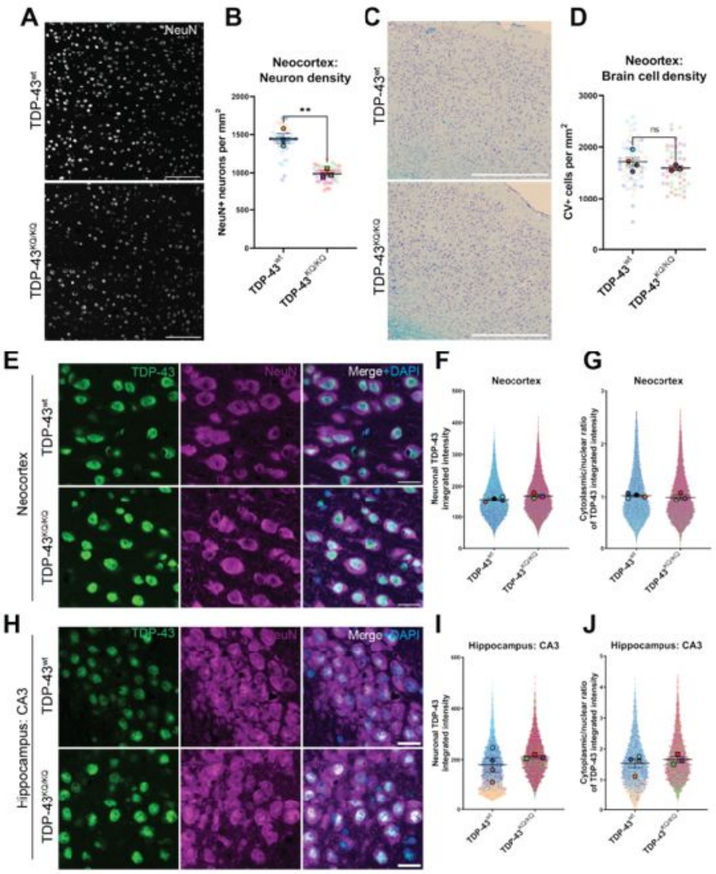

Figure 4

Neuronal loss in aged TDP-43$^{KQ/KQ}$ mice with retention of predominantly nuclear TDP-43.

A Representative confocal images of immunofluorescent labelling of NeuN+ neurons in the neocortex of 18-month TDP-43^{wt} or TDP-43$^{KQ/KQ}$ mice. **B** Quantification of NeuN+ neurons per square millimeter (mm) in TDP-43^{wt} and TDP-43$^{KQ/KQ}$ mice. **C** Representative widefield images of neocortex sections following Cresyl Violet (CV) labelling of endoplasmic reticulum Nissl substance. **E** Quantification of total brain cell density within the neocortex. **E,H** Representative confocal images of neocortex (**E**) and hippocampus (**H**) sections from 18-month-old TDP-43^{wt} and TDP-43$^{KQ/KQ}$ mice immunolabeled with TDP-43 (green), NeuN (magenta), and DAPI (blue). **F,I** Quantification of TDP-43 fluorescence intensity within NeuN+ neurons in the neocortex (**F**) or hippocampal CA3 region (**I**). **G,J** Quantification of the nuclear:cytoplasmic ratio of TDP-43 fluorescence intensity within NeuN+ neurons in the neocortex (**G**) and hippocampus (**J**). Scale bars = 100 μm (**A**), 500 μm (**B**), 20 μm (**E,H**). SuperPlots(87) show average value per animal in solid color bordered symbol (as mean ± SEM) over top of semi-transparent individual values from each animal. One color represents one animal. Individual datapoints in (**B**) and (**C**) represent density in a single field of view, with 10-16 fields across 4 brain sections per animal, n = 3-4 mice per genotype. Individual datapoints in **F-G** and **I-J** represent values from a single neuron within one field of view, with 1000-5000 neurons per animal across 12-16 fields from 4 (neocortex) or 2 (hippocampus) brain sections. Genotype comparisons by unpaired student's t-test. Statistical significance is represented by asterisks, **p<0.01; ns = not significant; unmarked = not significant.

We next examined the tissue for hallmarks of TDP-43 aggregation and did not detect prominent nuclear or cytoplasmic TDP-43 inclusions in the neocortex or hippocampus of TDP-43^{wt} or TDP-43$^{KQ/KQ}$ mice at 18 months of age. Since TDP-43 expression may be altered in FTLD-TDP and other TDP-43 proteinopathies(18),(84)–(86), we assessed TDP-43 immunoreactivity and abundance in NeuN-positive neurons in the neocortex and hippocampus, and then visualized the single-cell resolution data using SuperPlots(87). We observed trends of elevated TDP-43 protein in the neocortex and the CA3 region of the hippocampus (Fig. 4E-F, H-I) and also a potential subtle increase in the cytoplasmic to nuclear TDP-43 ratio within CA3 neurons (Fig. 4G, J). We note that these effects were not significant using microscopy and quantitative image analysis, which may result from technical challenges in achieving accurate image segmentation at the subcellular level needed to separate nuclear and cytoplasmic TDP-43 intensity within tissue samples. Therefore, to more reliably detect alterations in TDP-43 localization and solubility, we turned to an alternative biochemical approach of sequentially fractionating isolated hippocampus and neocortex tissue to generate soluble (RIPA-extracted) and insoluble (Urea-extracted) protein fractions. TDP-43$^{KQ/KQ}$ mouse neocortex harbored insoluble phosphorylated TDP-43 at the disease-associated Ser409/410 locus(88) (p409/410) at 12 months of age, which was even more prominent at 18 months (Fig. 5A, C), a timepoint at which TDP-43$^{KQ/KQ}$ mice show prominent behavioral and cognitive defects (Fig. 4). Notably, p409/410 immunoreactivity was minimal in the hippocampus of 12-month-old TDP-43$^{KQ/KQ}$ mice but increased dramatically by 18 months (Fig. 5D, F), coinciding with the onset of hippocampal-mediated learning deficits (Fig. 3C). Though p409/410 was elevated in TDP-43$^{KQ/KQ}$ mice, we were surprised to find that the total insoluble TDP-43 pool was not prominently altered, suggesting increases in TDP-43 phosphorylation may precede overt conversion towards insoluble TDP-43 accumulation.

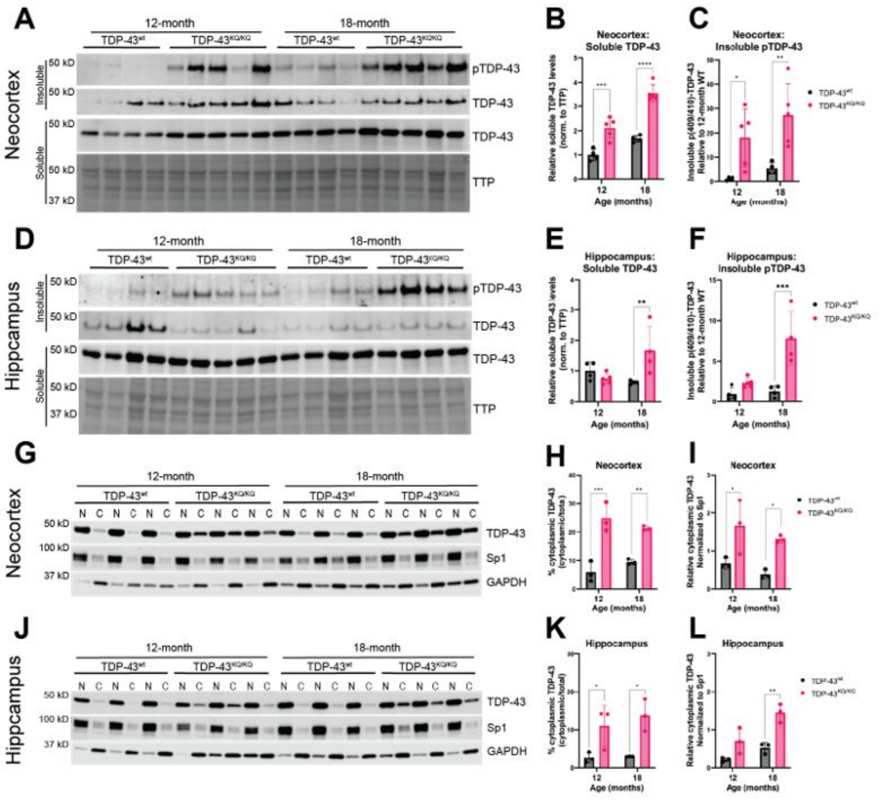

Figure 5

TDP-43 is hyper-phosphorylated and mislocalized in the neocortex and hippocampus of aged TDP-43$^{KQ/KQ}$ mice

A-F Western blot images comparing soluble and insoluble protein fractions in neocortex (**A**) and hippocampus (**D**) from TDP-43^{wt} and TDP-43$^{KQ/KQ}$ mice at 12- and 18-months of age. Quantification of soluble TDP-43 protein levels in neocortex and hippocampus tissue relative to total transferred protein (TTP) [neocortex (**B**) F (1, 14) = 97.67, p<0.0001; hippocampus (**E**) main effect of genotype F (1, 13) = 3.699, p=0.0766 and main effect of genotype*age interaction F (1,13) = 10.21, p=0.0070). Quantification of insoluble phosphorylated p(409/410)-TDP-43 levels in neocortex and hippocampus tissue [neocortex (**C**) F (1, 14) = 18.81, p=0.0007; hippocampus (**F**) F (1, 13) = 23.07, p=0.0003]. **G-I** Western blot images following isolation of soluble nuclear and cytoplasmic protein fractions from neocortex (**G**) and hippocampus (**J**) of TDP-43^{wt} and TDP-43$^{KQ/KQ}$ mice at 12- and 18-months of age. **J-L** Quantification of cytoplasmic TDP-43 measured as percent of total TDP-43 in neocortex and hippocampus [neocortex (**H**) F (1, 8) = 69.38, p<0.0001; hippocampus (**K**) F (1, 8) = 22.40, p=0.0015] and relative cytoplasmic mislocalization of TDP-43 after normalizing to cytoplasmic/nuclear ratio of the nuclear Sp1 protein in neocortex and hippocampus [neocortex (**I**) F (1, 8) = 19.79, p=0.0021; hippocampus (**L**) F (1, 8) = 29.94, p=0.0006]. **A-F** n=4 TDP-43^{wt} and n=5 TDP-43$^{KQ/KQ}$ at all ages and regions except 18-month hippocampus n=4 TDP-43$^{KQ/KQ}$. **F-L** n=4 all ages and regions. Data are presented as mean ± SD. Two-way ANOVA followed by Šídák's multiple comparisons test. **F** statistics represent the main effect of genotype unless otherwise stated. Statistical significance represented by asterisks, *p<0.05, **p<0.01, ***p<0.001, ****p<0.0001. Further statistical information is located Figure 5 Source Data 1 file.

We also examined soluble TDP-43 levels, as acetylation-induced loss of function may result in autoregulatory feedback that increases production of TDP-43(18). The soluble TDP-43 pool was significantly increased in TDP-43$^{KQ/KQ}$ at 12 months in the neocortex and at 18 months in both neocortex (Fig. 5A, B) and hippocampus (Fig. 5D, E), consistent with increases in autoregulated TDP-43 protein levels. To assess soluble TDP-43 localization using a biochemical approach, we performed subcellular fractionation to isolate nuclear and cytoplasmic proteins from the neocortex and hippocampus and found a striking increase in cytoplasmic TDP-43 in TDP-43$^{KQ/KQ}$ mice at both 12 and 18 months of age (Fig. 5G-L). The detection of hippocampal cytoplasmic TDP-43 at 12 months (Fig. 5J-L), which is not yet phosphorylated (Fig. 5D, F), suggests that cytoplasmic mislocalization occurs prior to TDP-43 phosphorylation(89),(90). Overall, our findings indicate that phosphorylated mislocalized TDP-43 coincides with neurodegeneration in TDP-43$^{KQ/KQ}$ mice, consistent with progressive FTLD-TDP(44).

Disease-linked transcriptomic and splicing defects are prevalent in acetylation-mimic TDP-43$^{KQ/KQ}$ mice

TDP-43 acetylation drives RNA dissociation and loss of TDP-43 function(52), implying that reduced RNA-binding capacity may impact transcriptional regulation and mRNA splicing(36),(50),(91). We performed total RNA sequencing on neocortex and hippocampus tissue from 18-month-old TDP-43^{wt} or TDP-43$^{KQ/KQ}$ mice to determine how TDP-43 acetylation affects RNA profiles *in vivo*. We identified nearly 400 differentially expressed genes (DEGs) in each brain region in TDP-43$^{KQ/KQ}$ mice compared to TDP-43^{wt}, after correcting for underlying batch effects. As expected by acetylation-induced loss of TDP-43 function and subsequent autoregulation, the *Tardbp* transcript was increased in both the hippocampus and neocortex **(Supplementary Tables S1, S2**). Follow-up RT-qPCR analysis confirmed a 2- to 3-fold increase in *Tardbp* expression in neocortex and hippocampus tissue (Fig. S8), which correlated with increased TDP-43 protein levels in these regions (Fig. 5B, E).

We then clustered the DEGs based on their up- or down-regulation and the brain region affected (Fig. 6), which revealed similar, but distinct, patterns of transcriptional alterations (Fig. 6, Fig. S9, **Supplementary Tables S1, S2**). To investigate the potential biological implications of the altered transcriptome, we performed Gene Ontology (GO) term enrichment analyses on DEGs identified in each of the six clusters, which revealed that similar pathways were affected in cortical and hippocampal tissues (**Supplementary Table S3**). In both brain regions, the most highly downregulated genes were involved in developmental processes, including many related to CNS development and maintenance, such as neurogenesis (e.g., *Sema5b, Rnd2, Brinp1*), gliogenesis (e.g., *Tlr2, Olig2, Sox10*), and myelination (e.g., *Nkx2-2, Nkx6-2, Sox10*). *Sema5b* was the most dramatically reduced transcript in the hippocampus, and the third most in the cortex, (**Supplementary Tables S1, S2**) with a two-fold reduction in expression in TDP-43$^{KQ/KQ}$ mice. Downregulated genes in both the hippocampus and neocortex were also enriched for terms related to synapse homeostasis and transmembrane signaling, however the dysregulated pathways were distinct. Genes related to GABAergic synapses (e.g., *Gad1, Gad2, Abat, Gnb5*) were selectively downregulated in the neocortex, while trans-synaptic signaling and ion transport mechanisms (e.g., *Homer3, Camk4a,Nsmf, Cnih2*) were decreased in the hippocampus.

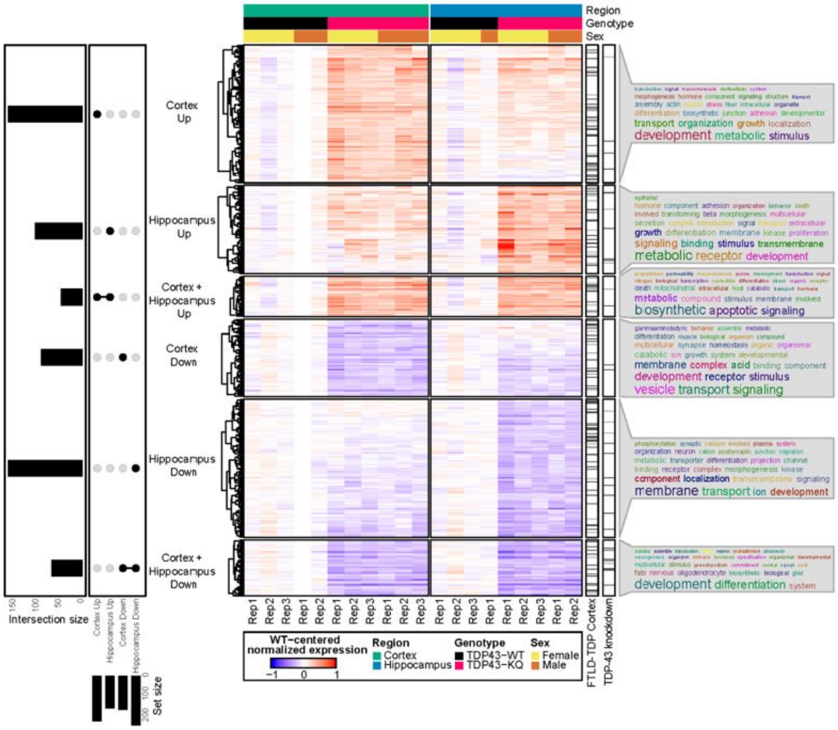

Figure 6.

RNA sequencing of aged TDP-43$^{KQ/KQ}$ mouse brain reveals dysregulation of neurodegeneration and FTLD-TDP-associated pathways

Genes differentially expressed between TDP-43$^{KQ/KQ}$ (TDP43-KQ) and TDP-43^{wt} (TDP43-WT) cortex and hippocampus were compared and their intersections were defined as 6 gene groups, as represented by an UpSet plot (left). Normalized gene expression values, centered around the mean of TDP-43^{wt} samples for each brain region, were then hierarchically clustered and plotted as a heatmap (center, red indicates expression higher than that of WT, blue indicates expression lower than WT). Genes that were significantly altered in human FTLD-TDP temporal and/or frontal cortex (Hasan et. al.(92), “FTLD-TDP Cortex” bar), or striatal mouse brain TDP-43-knockdown (Polymenidou et al.(93), “TDP-43 knockdown” bar) were demarcated with tick marks. Each gene group was assessed for over-enrichment of Gene Ontology terms and these results were summarized as word clouds (right). Neocortex n=5 TDP-43^{wt}, n=6 TDP-43$^{KQ/KQ}$; hippocampus n=4 TDP-43^{wt}, n=5 TDP-43$^{KQ/KQ}$.

In contrast, there was significant upregulation of cellular stress response genes (*Sesn1*, *Nrros*, *Plat*, *Klf15*) and many apoptotic regulators (e.g., *Trp53inp1*, *Pmaip1*, *Bcl2l1*, *Plekhf1*) in both the hippocampus and neocortex, along with an over-representation of GO terms related to metabolism, localization, cell adhesion (Fig. 6, Supplementary Table S3). Several pathways were uniquely altered, however, suggesting brain region-specific transcriptional effects of acetylation-mimic TDP-43 in TDP-43$^{KQ/KQ}$ mice. For example, coagulation and complement cascades were only upregulated in the hippocampus (e.g., *F3, Plat, CD59a*). Intriguingly, while genes associated with trans-synaptic signaling were decreased in the hippocampus, another set of genes involved in this same pathway was upregulated in the cortex (*e.g.,Syt7*, *Synpo*, *Nptx1*, *Spg11*) (**Supplementary Table S3**).

Given the cognitive defects in TDP-43$^{KQ/KQ}$ mice, we sought to draw parallels between the TDP-43$^{KQ/KQ}$ mouse and human FTLD-TDP transcriptome. Comparison of the DEGs in TDP-43$^{KQ/KQ}$ mice to the mouse orthologs of those found in FTLD-TDP frontal or temporal cortex tissue(92) revealed marked overlap between our mouse and their human data sets (Fig. 6, see “FTLD-TDP Cortex” bar), particularly in the hippocampus (**Supplementary Table S4**; p = 0.0003 "Hippocampus Down" vs Downregulated in FTLD-TDP frontal cortex; p = 0.0014 "Hippocampus Down" vs Downregulated in FTLD-TDP temporal cortex; p = 0.0048 "Hippocampus Up" vs Upregulated in FTLD-TDP frontal cortex). A similar alignment comparing DEGs in mouse striatum following TDP-43 knockdown(93) also identified commonly altered genes, particularly in the TDP-43$^{KQ/KQ}$ downregulated gene sets (Fig. 6, see “TDP-43 knockdown” bar; **Supplementary Table 4**; p = 0.019 "Hippocampus Down" vs Downregulated in TDP-43-KD; p = 0.046 "Cortex Down + Hippocampus Down" vs Upregulated in TDP-43-KD). Together, this data defines distinct functional signatures including altered synaptic gene expression and stress response signaling that are reflective of acetylation-induced TDP-43 dysfunction and the progression of FTLD-TDP.

Alternative splicing defects, particularly impaired repression of cryptic exons, due to TDP-43 dysregulation are implicated in FTLD and ALS pathogenesis(94)–(99). In line with our findings above that TDP-43$^{KQ/KQ}$ primary cortical neurons *in vitro* show splicing deficits (Fig. 2E-F), we identified widespread splicing alterations *in vivo*. Analysis of TDP-43$^{KQ/KQ}$ mouse neocortex samples identified 289 differentially spliced genes (DSGs), with 81.7% of loci containing at least one cryptic splice junction, and 29.8% containing two cryptic splice junctions (**Supplementary Table S5**). In the hippocampus, we found 126 DSGs, 77.0% of which contain a cryptic splice junction and 41.3% that are formed by two cryptic splice sites (**Supplementary Table S6**). The alternative splicing events were relatively consistent between brain regions, as over 70% of the DSGs identified in the hippocampus were also present in the cortex. Among the most significant DSGs identified were several known TDP-43 splicing targets (e.g., *Kcnip2*, *Pdp1*, *Poldipp3*, *Ppfibp1*, *Dnajc5. Tmem2, Sort1*)(24),(93),(95), transcripts associated with particular neurodegenerative diseases (e.g., *Mapt, Atxn1, Lrrk2*) (100)–(106), and also many robustly altered transcripts that are not well-characterized but have been linked to neurodegeneration (e.g., *Nrxn3, Nos1, Arfgef2, Arhgap10, Lrp8, Smarca4, Rims2*). Of all identified DSGs, the most substantially altered transcript was *Sort1*, encoding the Sortilin-1 (SORT1) protein. Exclusion of an exon toward the 3’ end of the *Sort1* transcript was reduced by 55.9% in TDP-43$^{KQ/KQ}$ cortex and by 57.0% in the hippocampus (Fig. 7A, B), such that in both tissues the aberrant *Sort1* transcript was the predominant variant detected via RNA sequencing.

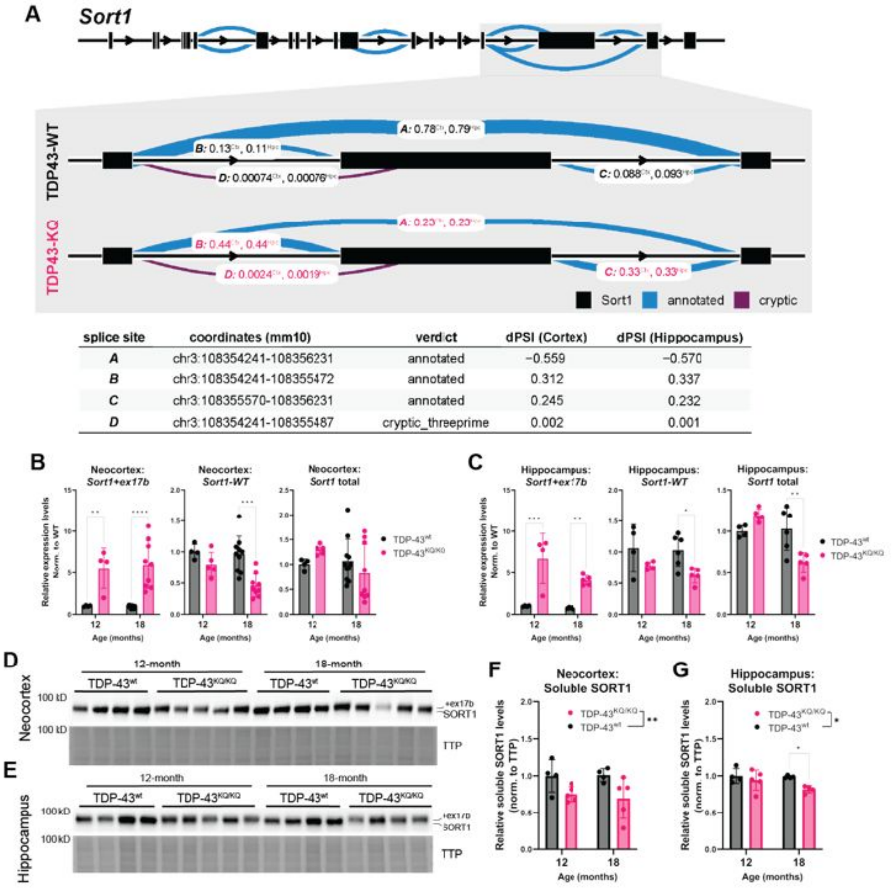

splice site	coordinates (mm10)	verdict	dPSI (Cortex)	dPSI (Hippocampus)
A	chr3:108354241-108356231	annotated	−0.559	−0.570
B	chr3:108354241-108355472	annotated	0.312	0.337
C	chr3:108355570-108356231	annotated	0.245	0.232
D	chr3:108354241-108355487	cryptic_threeprime	0.002	0.001

Figure 7.

Dysfunctional splicing regulation of the *Sort1* transcript in TDP-43$^{KQ/KQ}$ mice

A Differential splicing analysis of TDP-43^{wt} and TDP-43$^{KQ/KQ}$ neocortex ("Ctx") and hippocampus ("Hpc") using LeafCutter(180) (visualized with LeafViz(181)) demonstrates reduction in exclusion of a late cryptic exon within the *Sort1* transcript. Diagram in (**A**) shows full-length *Sort1* gene in upper panel and highlights the differentially spliced region in gray. Chromosomal location, intron start and end points, annotation status, and Δ percent spliced in (dPSI) of the intronic region is listed in the lower table. **B-C** qPCR analysis of additional WT and TDP-43$^{KQ/KQ}$ neocortex (**B**) and hippocampus (**C**) samples using primers specific for *Sort1* splice variants [neocortex *Sort1-ex17b* F (1, 23) = 35.64 p<0.0001, *Sort1-WT* F (1, 24) = 15.22 p=0.0007, *Sort1* total F (1, 25) = 0.01856 p=0.8927; hippocampus *Sort1-ex17b* F (1, 14) = 44.33 p<0.0001, *Sort1-WT* F (1, 15) = 9.798 p=0.0069, *Sort1* total F (1, 16) = 2.086 p=0.1679]. **D-G** Images of western blots probed for SORT1 protein from neocortex (**D**) and hippocampus (**E**) lysates from 12- and 18-month-old mice. The SORT1 protein band intensity is plotted relative to total transferred protein (TTP) and quantified in **F-G** [neocortex, F(1,14)=9.308, p=0.0086; hippocampus, F(1,13)=6.117, p=0.0280]. Neocortex n=5 TDP-43^{wt}, n=6 TDP-43$^{KQ/KQ}$; hippocampus n=4 TDP-43^{wt}, n=5 TDP-43$^{KQ/KQ}$. Data are presented as mean ± SD. Two-way ANOVA followed by Šídák's multiple comparisons test. F statistics represent main effect of genotype, unless otherwise stated. Statistical significance is represented by asterisks, *p<0.05, **p<0.01, ***p<0.001, ****p<0.0001. Further statistical information is located Figure 7 Source Data 1 file.

SORT1 is a highly expressed neurotrophic factor receptor that binds progranulin (PGRN) and regulates endosomal/lysosomal function through a pathway that is genetically linked to FTLD-TDP(107)–(111). Recent studies suggest that TDP-43 depletion results in inappropriate inclusion of the *Sort1* exon 17b and production of a soluble and putatively toxic SORT1 variant that is increased in FTLD-TDP patients(93),(112),(113). To confirm that the altered splicing in our sequencing data was *Sort1* exon 17b inclusion, we performed qPCR using primers specific for the mouse *Sort1+ex17b* transcript, the appropriately spliced variant (*Sort1-WT*), and all *Sort1* variants (*Sort1* total) on tissues isolated from TDP-43$^{KQ/KQ}$ or WT mice(113). This analysis showed a nearly 8-fold increase in the *Sort1+ex17b* transcript in the cortex (Fig. 7C) and hippocampus (Fig. 7D) of both 12- and 18-month-old animals, which is accompanied by an approximately 25% decrease in *Sort1-WT* transcripts. Interestingly, the total level of *Sort1* transcript varied with age, with slightly increased levels at 12 months and reduced levels at 18 months of age, suggestive of a negative feedback mechanism regulating *Sort1* expression.

To determine whether the *Sort1+ex17b* transcript identified in TDP-43$^{KQ/KQ}$ mice might generate a distinct SORT1 protein, we immunoblotted hippocampus and cortex homogenates and identified a higher molecular weight SORT1 in TDP-43$^{KQ/KQ}$ compared to WT mice (Fig. 7E, F), consistent with *Sort1* exon 17b inclusion. Notably, this abnormal SORT1 protein showed decreased stability in TDP-43$^{KQ/KQ}$ mice, as suggested by reduced protein levels in acetylation-mimic animals, compared to controls (Fig. 7G, H). These data indicate failure to repress cryptic exon inclusion and an altered SORT1-PGRN axis, indicating an aberrant splicing pattern in TDP-43$^{KQ/KQ}$ mice that resembles alterations seen in human FTLD-TDP.

Discussion

Here, we show that a TDP-43 acetylation-mimic mutation that disrupts RNA binding (TDP-43^{K145Q}) is sufficient to recapitulate TDP-43 dysfunction using a combination of biochemical, molecular, and behavioral analyses. Our knock-in TDP-43^{K145Q} mice showed impaired learning and cognition, as well as behavioral disinhibition with age, which are representative of an dementia or FTLD-like neurodegenerative phenotype. The progressive age-dependent behavioral defects and parallel increases in insoluble phosphorylated TDP-43 in the neocortex and hippocampus of TDP-43$^{KQ/KQ}$ mice are consistent with age acting as a primary risk factor and putative trigger for the pathogenic effects of aberrant TDP-43. Lastly, we show significant transcriptomic alterations in aged mice expressing aberrant TDP-43, including abnormal splicing activity and upregulation of stress response and neurodegeneration-associated pathways. Our findings indicate that disrupted RNA binding due to TDP-43 acetylation within RRM domains contributes to the pathogenesis of TDP-43 proteinopathies and the evolution of a dementia-like syndrome.

Assessment of neurodegeneration in this acetylation-mimic mouse model revealed that 18-month-old TDP-43$^{KQ/KQ}$ animals have reduced neuronal density in the neocortex without a significant decline in total brain cell density in this region. Intriguingly, this occurs without substantial astro- or microgliosis as assessed by measurements of GFAP or Iba1 fluorescence, respectively. The role of neuroinflammation in this model remain to be determined, as does the composition of the non-neuronal, non-astrocytic, non-microglial cells that seem to reside in aged TDP-43$^{KQ/KQ}$ neocortex. Potential components of this cell population include oligodendrocytes and infiltrating peripheral immune cells, as both have been implicated in the neurodegenerative process and in TDP-43 proteinopathies(114)–(118). Future studies are warranted to better understand the potential neurodegenerative and neuroinflammatory phenotype in the TDP-43$^{KQ/KQ}$ mouse model.

Our prior mass spectrometry analysis identified acetylated lysines K145 and K192(52), while a more recent study identified residues K84 (within the NLS) and K136 (within RRM1) as additional lysine residues of interest(66). It is likely that acetylation within the RRMs impairs TDP-43 function, as multiple studies have shown that acetylation mimic TDP-43^{K136Q} or TDP-43^{K145Q} variants phenocopy one another, with both showing nuclear foci (or anisosome) formation and reduced RNA binding. This suggests that deficient RNA binding may explain why acetylation, or acetylation-mimic mutations within RRM1, alter TDP-43 dynamics and cause pathology. RNA-binding deficient TDP-43, including variants with RRM mutations or deletions, showed increased TDP-43 phase separation, aggregation, nuclear egress, and neurotoxicity(34),(58),(63),(66). Conversely, enhancing RNA binding mitigates these phenotypes(67),(119),(120), likely in large part due to TDP-43 retention within the nucleus(36). We hypothesize that the reduced nucleic-acid binding capacity of acetylation-mimic TDP-

43^{K145Q} is responsible for the TDP-43 mislocalization, aggregation, and RNA dyshomeostasis observed in our model, and the neurotoxicity and deficits these impart. Thus, impaired RNA binding achieved by K145 acetylation, or other RRM domain modifications, may promote pathogenesis of TDP-43 proteinopathies.

Acetylated TDP-43 (detected with an acetylation-specific ac-K145 antibody) is found within ALS spinal cord inclusions and has not yet been detected in FTLD-TDP cortex(52), however pathology in these cases is dominated by C-terminal fragments lacking RRM1 thereby precluding detection of the acetylated K145 site(54),(121). It is possible that TDP-43 acetylation still occurs in FTLD at one or more lysine residues, thus future mass spectrometry studies will be needed to determine whether TDP-43 acetylation occurs in earlier in the progression of FTLD-TDP. While the precise physiological or cellular role for TDP-43 acetylation remains unclear, given its impact on RNA binding, one can imagine TDP-43 acetylation may fine-tune TDP-43's normal cellular processes, and in conjunction with other disease risk factors such as aging, drive vulnerable neuronal populations toward degeneration.

Consistent with acetylation-induced loss of function, the $TDP\text{-}43^{KQ/KQ}$ mice show striking similarities to other TDP-43 depletion models. For example, the RNA profiles in $TDP\text{-}43^{KQ/KQ}$ brain, particularly the hippocampus, were similar to a mouse model of striatal TDP-43 knock down (Fig. 6), including upregulation of immune response genes (*Serpine1*, *Serping1*) and altered splicing of TDP-43 targets (*Kcnip2*, *Sort1*, *Dnajc5*, *Pdp1*, *Poldip3*)(93). Similar splicing deficits were found in conditional CAMKIIa-driven *Tardbp* knockout mice, accompanied by an FTLD-like phenotype with disinhibitory behavior and spatial learning deficits resembling those seen in $TDP\text{-}43^{KQ/KQ}$ mice(122),(123). Hippocampal knockdown of TDP-43 in adult mice impaired learning and memory, likely due to synaptic loss(124). Together, these findings imply that acetylation-induced TDP-43 loss of function imparts neurotoxicity and neurodegeneration. However, unlike $TDP\text{-}43^{KQ/KQ}$ mice, complete TDP-43 depletion is not viable(23),(125), and therefore the K145Q substitution creates a powerful yet viable model that cannot represent a complete loss of function, as these mice do not display developmental defects or ALS-like motor phenotypes (at least up until 18 months old), nor does their expression profile entirely align with striatal TDP-43 knockdown(93). This is likely in part because $TDP\text{-}43^{K145Q}$ maintains some level of RNA binding capacity, leaving some TDP-43-dependent processes unperturbed. In turn, acetylated TDP-43 may also impart gain-of-function toxicity due to altered RNA binding patterns and conformational instability, leading to nuclear export, enhanced phosphorylation and aggregation, and a dysregulated transcriptome, as we observe in $TDP\text{-}43^{KQ/KQ}$ mice. As both loss- and gain-of-function effects have been proposed for familial disease-causing *TARDBP* mutations(45),(46),(95),(126), we hypothesize that $TDP\text{-}43^{K145Q}$ acts in a similar manner, which is supported by our present findings.

RNA sequencing revealed profound transcriptomic alterations within aged $TDP\text{-}43^{KQ/KQ}$ mouse brains. Many up- and down-regulated transcripts identified in acetylation-mimic mice were also differentially expressed in FTLD-TDP human tissue (Fig. 6), particularly genes associated with cellular stress response, synaptic regulation, apoptotic signaling, and cellular adhesion(92),(127), representing potential FTLD-TDP pathomechanisms. Disease-related alternative splicing events were also common within $TDP\text{-}43^{KQ/KQ}$ cortex and hippocampus. For example, the altered splicing of *Sort1* and subsequent generation of *Sort1+ex17b* we observed in TDP-43 acetylation-mimic mice (Fig. 7), is also found in FTLD-TDP brain samples(108),(113). Moreover, SORT1 facilitates the endocytosis and lysosomal degradation of PGRN(108),(110), a protein whose deficiency is causative of 10-30% familial FTLD cases(128)–(130). In humans, SORT1+ex17b contains an additional proteolytic site, resulting in the production of a soluble toxic variant that impairs the function of SORT1, prevents binding to PGRN and impacts neuronal survival(107),(113). A recent study showed that TDP-43 depletion increased SORT1+ex17b, impaired brain derived neurotrophic factor (BDNF) signaling, and reduced synaptic plasticity in mice(112). We speculate that acetylated TDP-43 alters SORT1/PGRN signaling, contributing to the synaptic dysregulation that is so evident in our transcriptome data. Future mechanistic studies are aimed at interrogating PGRN signaling in TDP-$43^{KQ/KQ}$ mice.

Other aberrantly spliced transcripts in TDP-$43^{KQ/KQ}$ mice provide additional insight into novel pathogenic mechanisms. The synaptic regulators *Arfgef2*(131) and *Arhgap10*(132),(133) were among the most affected transcripts. Concurrently, *Sema5b* which regulates synaptic connections and axon guidance(134)–(137), was strongly downregulated in in TDP-$43^{KQ/KQ}$ hippocampus and cortex, as were other genes involved in synapse homeostasis and signaling. Interestingly, *Argef2* and *Arghap10* are also known to regulate apoptosis(131),(132), suggesting the observed neuronal loss in TDP-$43^{KQ/KQ}$ cortex may occur via the upregulation of apoptosis-related transcripts. Furthermore, splicing of LRP8 (low-density lipoprotein receptor-related protein 8) was significantly altered in TDP-$43^{KQ/KQ}$ mice, and abnormalities in LRP8 can cause learning and memory defects, likely by disrupting Reelin-mediated synaptic plasticity and long-term potentiation (LTP)(138)–(141). Similarly, *Nos1*, encoding the neuronal nitric oxide synthase (nNOS) protein that regulates LTP and synaptic plasticity via the production of nitric oxide(142),(143), showed aberrant splicing patterns in TDP-$43^{KQ/KQ}$ mice. Importantly, all of these synaptic regulators (*Nos1*, *Lrp8*, *Argef2*, *Sema5b*) and other significantly altered splice variants (e.g., *Adipor2*, *Mapk14*, *Smarca4*, *Sort1*, *Mapt*) have all been linked to AD and other neurodegenerative diseases(101),(141),(143)–(151). Altogether, our transcriptome data strongly suggests that splicing and transcriptional abnormalities due to TDP-43 acetylation impacts synaptic plasticity, neurotransmission, and neuronal survival pathways in the TDP-$43^{KQ/KQ}$ model, which overlaps with abnormalities found in human FTLD-TDP patients.

In conclusion, disrupting RNA-binding with an acetylation mimic TDP-43^{K145Q} mutation results in an age-dependent, dementia-like neurodegenerative phenotype characterized by many signatures of FTLD, including progressive cognitive deficits, TDP-43 mislocalization and phosphorylation, and prominent RNA dysregulation. Interrogation of the affected genes linked TDP-43 acetylation to many known FTLD-associated pathways, including SORT1-PGRN and stress response signaling, while also pinpointing new putative factors as mediators of disease pathogenesis. Thus, by developing new human and mouse models of TDP-43 acetylation, we expanded our understanding of sporadic TDP-43 proteinopathies and provide a valuable model in which to identify and test new avenues for therapeutics that target the TDP-43 proteinopathy pathogenic cascade.

Methods

Animal Husbandry

Mice were housed in ventilated microbarrier cages on racks providing HEPA filtered air supply to each cage. Animals were kept on a 12hr light-dark cycle with access to food and water *ad libitum*. All animal husbandry, experiments, and procedures were performed in strict compliance with animal protocols approved by the Institutional Animal Care and Use Committee (IACUC) of the University of North Carolina at Chapel Hill (Protocol #21.257).

Primary neuron cultures

Murine primary cortical neurons were performed using wild-type C57Bl/6 mice (Charles River) or TDP-$43^{wt/KQ}$ breeding pairs. Timed pregnant females at embryonic day 15-16 were lethally anesthetized with isoflurane. The abdominal cavity was opened, and the uterus incised to remove the placentas and embryonic sacs, which were washed briefly in ice-cold 70% ethanol and then placed in cold HEPES-buffered Bank's balanced salt solution (HBSS). The embryos were transferred into a 10cm dish containing cold HBSS, the embryos removed from the amniotic sac, and the brains were extracted from the cranium. For TDP-43$^{wt/KQ}$ dissections, process was paused for approximately 2 hours to permit genotyping of the fetuses, during which the brains were stored at 4° C protected from light in a Hibernate-E (BrainBits NC9063748) solution supplemented with B27 (Gibco 17504044) and GlutaMAX (ThermoFisher 35050061). After genotyping, if applicable, the cerebral cortices from each brain were isolated under a stereomicroscope, pooled by genotype, minced with forceps, and digested for 30min at 37°C in a filter-sterilized HBSS solution containing 20U/mL papain (Worthington Biochemical LS003126), 1mM EDTA, 0.2mg/mL L-cysteine, and 5U/mL DNAse (Promega M6101). The enzyme solution was removed, and the digested tissue was washed twice with sterile HBSS. Warm plating media [BrainPhys media (Stemcell 05790), 5% fetal bovine serum, 1x penicillin/streptomycin (Gibco 15140122), 1x B27, 1x GlutaMAX] containing 5U/mL DNAse, was added and the tissue was dissociated mechanically using a P1000 pipette. The resulting cell suspension was spun down for 5min at 1.5rcf to pellet the cells, resuspended in plating media, and filtered through a 40 mm cell strainer. Cells were counted using a hemocytometer and plated onto poly-D-lysine (PDL)-coated 12-well tissue culture plates (Corning 356470) at 300K cells/well (for RNA extraction) or 96-well glass bottom black wall plates (Cellvis P96-1.5H-N) at 30K/well (for immunofluorescence and microscopy). 16-24hours after plating, all plating media was removed and replaced with neuronal cell media (BrainPhys, 1x GlutaMAX, 1x B27, 1x penicillin/streptomycin). Cultures were incubated at 37°C, 5% CO^2 and 95% humidity with half-media exchanges every 3 days for the duration of all experiments.

Lentivirus preparation and neuron transduction

Lentiviral vectors were constructed in-house using the pUltra vector as a backbone for cloning via restriction enzyme digestion followed by ligation. The pUltra construct was acquired from Addgene (gift from Malcolm Moore; Addgene plasmid # 24129 ; http://n2t.net/addgene:24129 ; RRID:Addgene_24129)(152). To generate TDP-43 constructs, TDP-43 variant gene fragments were PCR amplified using TDP-43 F' and R' primers (Supplementary Table 7) and a pcDNA5/TO-myc-TDP-43^{wt}, - myc-TDP-43^{K145Q,} or -myc-TDP-43^{K145R} plasmid(52) as the template. The pUltra construct was digested with AgeI and BamHI, and then incubated with the appropriate TDP-43 PCR product in the presence of T4 DNA ligase and T4 Polynucleotide Kinase for 1 hour at room temperature. The resulting ligation product was transformed into NEB stable competent cells using standard protocols.

To generate the hSyn-IBB-GFP-mCherry3E construct, we isolated the IBB-GFP-mCherry3E coding sequence from pHBS1389-IBB-GFP-mCherry3E (gift from Rajat Rohatgi; Addgene plasmid # 118803 ; http://n2t.net/addgene:118803 ; RRID:Addgene_118803)(68),(153) via digest with AgeI and XhoI. In addition, the pUltra Ubc promoter was excised by PacI and AgeI digestion, and the hSyn promoter sequence was inserted via ligation as described above to generate a hSyn-eGFP construct. Finally, the eGFP of hSyn-eGFP was removed with AgeI and SalI digestion and then replaced by incubation with the IBB-GFP-mCherry3E fragment in the presence of T4 DNA ligase and T4 Polynucleotide Kinase for 1 hour at room temperature. The resulting ligation product was transformed into NEB stable competent cells using standard protocol.

Lentiviral production was performed by co-transfecting (CalPhos™ Mammalian Transfection Kit, TakaRa 631312) 37.5 µg lenti-plasmid with 25 µg psPAX2, 12.5 µg VSVG, and 6.25 µg REV for each 15 cm dish of lenti-X 293T cells (Takara 632180) and 3 dishes of cells were used for each lentiviral production. 3 days after transfection, culture media were collected and centrifuged at 2000g for 10 min. Lentiviral particles were purified using a double-sucrose gradient method. Briefly, the supernatants were loaded onto a 70%-60%-30%-20% sucrose gradient and centrifuged at 70,000g for 2 hr at 17°C (Beckman Optima LE-80K Ultracentrifuge, SW 32 Ti Swinging-Bucket Rotor). The 30%-60% fraction containing the viral particles was retrieved, resuspended in PBS, filtered with a 0. 45μm filter flask before loaded onto a 20% sucrose cushion, and centrifuged a second time at 70,000g for 2 hr at 17°C. The supernatants were carefully discarded, and the viral particles present in the pellet were resuspended in PBS, aliquoted and stored at -80°C.

Lentivirus aliquots were evaluated for neuronal transduction ability prior to each experiment and diluted to approximately equal concentrations of effective virus. Lentiviral transductions were performed on DIV10 for a DIV14 harvest or DIV24 for a DIV28 harvest. In brief, lentiviruses were diluted to a 2x concentration in neuronal media, and then added to plates via half-media exchange. 24 hours after viral transduction, all virus-containing media was removed and replaced with 50% fresh neuronal media and 50% conditioned media from plates containing WT non-transduced neurons. Neurons were then cultured to DIV14 or DIV28 as the experiment required.

hiPSC-derived cortical neurons

iPSC maintenance: The HPC26 iPSCs were maintained on Matrigel-coated dishes (Corning 354480) in StemFlex Medium (Thermo FisherScientific A3349401) and passaged every 3-4 days with 0.5 mM EDTA dissociation solution as previously described(154).

CRISPR/Cas9 genome editing: We used a control wildtype HPC26 cell line(154) to generate two separate point mutations in the TARDBP gene that encodes the TDP-43 protein. Both mutations created single amino acid substitutions to change lysine 145 to glycine or arginine (K145Q and K145R). Benchling was used to design two guide RNAs and the corresponding single-stranded DNA donor oligos. The guide RNAs were purchased from Synthego, and the donor oligos from IDT. Genome editing was performed as described in Battaglia et. al(155). Briefly, $3x10^5$ iPSCs were electroporated on the Neon electroporation system (Thermo Fisher Scientific) with recombinant protein complexes made of Cas9 v2 protein (Thermo Fisher Scientific A36498), 900 ng sgRNA-TARDBP and 2700 ng of single-stranded donor oligonucleotide-K145Q or donor oligonucleotide-K145R (Supplementary Table 7). Seventy-two hours after electroporation, cells were plated for single cell screening on a 96-well plate format using the limited dilution method. After two weeks, single cells were expanded, genome DNA collected and the exon 4 of TARDBP amplified using the specific primers Ex4Fr and Ex4Rv (Supplementary Table 7). Screening for single or double allele gene edits was perform by Sanger sequencing (Fig. S2a-c).

Characterization of edited iPSC clones: Stemness edited iPSCs was assessed by immunofluorescent staining of the pluripotency factors OCT4, SOX2, SSEA4 and Tra-1-60 using specific antibodies (Supplementary Table 8) as described(154) (Fig. S2d-e). To confirmed stemness and differentiation capabilities of the edited iPSCs we used the Taqman hPSC Scorecard (ThermoFisher A15871) as described in Battaglia et al(155). Briefly, iPSCs were differentiated into all three germ layers using STEMdiff Trilineage Differentiation Kit (StemCell Technologies), a mono-layer based protocol to directly differentiate hES cells in parallel into the three germ layers. Non-differentiated and differentiated cells were lysed and total RNA purified using the RNeasy kit (QIAGEN 74004). RNA reversed transcription was performed with the high-capacity cDNA Reverse Transcription kit (ThermoFisher 4368813) following the Taqman Scorecard's manufacture guidelines. qRT-PCR was carried out using the QuantStudio 7 Flex Real-Time PCR system. The TaqMan PCR assay combines DNA methylation mapping, gene expression profiling, and transcript counting of lineage marker genes(156).

iPSC-derived cortical neurons: We adapted, modified and standardized a protocol to generate mature cortical neurons from iPSCs using a dual SMAD inhibition protocol(157),(158). First, undifferentiated iPSCs were collected with Accutase, counted and $3x10^5$ cells cultured in StemScale PSC medium (A4965001) supplemented with 10 µM Y27632 (PeproTech 1293823) and cultured in suspension on an orbital shaker at 37 C and 5% CO^2. After 48 hours, cells were dissociated with Accutase and $3x10^5$ cells differentiated into NPCs as neutrosphere in StemScale PSC medium supplemented with 10 µM Y27632 (PeproTech 1293823) and 1.5 µM CHIR99021 (PeproTech 2520691),10 µM SB431542 (PeproTech 3014193) and 50 nM LDN-193189 (Sigma SML0755). CHIR99021 was removed after 24 hours and cells were cultured for 10 days with daily medium changes and neurospheres dissociated at 1:3 ratio twice a week. Then NPCs were expanded for 7 days in the presence of 20 ng/ml FGF (Peprotech 100-18B) in Neuronal Expansion Medium [1:1 Advanced DMEM/F12 (12634028) and Neural Induction Supplement (A1647801)]. NPCs were plated for maturation on PDL/Laminin coated plates or coverslips in cortical neuron maturation medium [1:1 Advanced DMEM/F12 and Neurobasal; 1X GlutaMAX, 100mM B-mercaptoethanol, 1x B27, 0.5x N2, 1x NEAA and 2.5 mg/ml insulin (Sigma-Aldrich I9278)] supplemented with 10 ng/ml BDNF, 10 ng/ml GDNF, and 10 uM DAPT. Seventy-two hours after plating, cells were treated with 1 µg/ml Mitomycin C for (Sigma M5353) for 1 hour. Cellular identity was assessed specific markers of neuronal progenitor (PAX6, SOX2, and SOX1), and mature neurons (MAP2, TUJ1, CTIP2 and SATB2) (Fig. S3) (Supplementary Table 8). All reagents were purchased from ThermoFisher unless otherwise noted.

Primary mouse neuron and hiPSC-derived cortical neuron arsenite treatments and immunocytochemistry

On DIV14 (mouse primary neurons) or mature hiPSC-derived cortical neurons (~DIV50), neurons were treated for 2 hours with 200µM sodium arsenite ($NaAsO^2$) or vehicle (molecular biology grade water). Following treatment, neurons were fixed with 4% paraformaldehyde (PFA) in 1x phosphate buffered saline (PBS) and washed with 1xPBS. Neurons were permeabilized with 0.3% Triton X-100 in 1xPBS for 15min at RT, blocked in an 8% normal goat serum (NGS) 0.2% Triton X-100 in 1xPBS solution for 1-2 hours at RT, and incubated with primary antibodies (Supplementary Table 8) diluted in 4% NGS, 0.2% Triton X-100, 1xPBS solution overnight at 4°C. The next day, the neurons were washed with 1xPBS, followed by application of fluorescent secondary antibodies (Supplementary Table 8) diluted in 4% NGS, 0.2% Triton X-100, 1xPBS solution for 2 hours at RT, covered. Cells were washed four times with 1xPBS, with the third wash containing 1µg/mL 4',6-Diamidine-2'-phenylindole dihydrochloride (DAPI). 96-well plates were preserved in an 85% glycerol in 1xPBS solution containing 0.4% sodium azide for microbial prevention. Coverslips were mounted onto pre-cleaned glass slides using ProLong^{TM} Diamond Antifade Mountant (Invitrogen P36961).

Cultured neuron fluorescence microscopy and image analysis

Mouse primary cortical neurons in 96-well plates were visualized via automated fluorescence microscopy using EVOS M7000 Imaging System (ThermoFisher AMF7000) equipped with Olympus 20x/0.75 NA UPlanSApo and Olympus 40x/0.95 NA UPlanSApo objectives, and the following filter cubes: DAPI (357/44 nm Excitation; 447/60 nm Emission), GFP (482/25 nm Excitation; 524/24 nm Emission), Texas Red (585/29 nm Excitation; 628/32 nm Emission), and Cy5.5 (655/40 nm Excitation; 794/160 nm Emission). Images were acquired in an automated fashion, using DAPI fluorescence as the autofocus substrate, taking 16-32 images per well of 2-3 wells per experimental condition. Automated quantitative image analysis was performed using CellProfiler 4.0(159),(160) to measure TDP-43 fluorescence intensity within neuronal compartments and to count TDP-43-positive foci within neurons. To identify neurons and subcellular compartments, DAPI was used to delineate nuclei and NeuN was used to label neuronal soma. hiPSC-derived cortical neurons were imaged on a Leica SP8X Falcon confocal microscope equipped with a 63x/1.40 NA Plan Apochromatic (oil) objective and hybrid GaAsP detectors, Leica Application Suite X Life Sciences software (Leica, Wetzlar, Germany).

Primary neuron splicing function assays

Primary cortical neurons were cultured and transduced with the hSyn-IBB-GFP-mCherry3E CFTR splicing reporter at DIV10 or DIV24, as described above. For RT-PCR experiments, neurons were washed with 1xPBS and harvested on DIV14 and DIV28, and RNA was extracted using the Qiagen RNeasy mini kit (Qiagen, Inc. 74106) with on-column DNAse digestion per manufacturer's instructions. RNA concentration was determined using a NanoDrop 2.0 spectrophotometer, 250ng of RNA was used to generate cDNA using Applied Biosystems High-capacity RNA-to-cDNA kit (#4387406) per manufacturer's instructions. PCR was performed using GoTaq Green Master Mix (Promega M7122) and the Cryptic Exon F' and Cryptic Exon R' primers (Supplementary Table 7). PCR products were separated on a 2% agarose Tris-acetate-EDTA gel containing SybrSafe stain (Invitrogen S33102) and visualized on an ImageQuant LAS4000 machine. Band intensities were quantified using LI-COR Image Studio Lite.

Mouse model generation and genotyping

CRISPR/Cas9 Reagents

Cas9 guide RNAs targeting the mouse *Tardbp* K145 codon were identified using Benchling software (Benchling, San Francisco, CA, USA). Three guide RNAs were selected for activity testing. Guide RNAs were cloned into a T7 promoter vector followed by in vitro transcription and spin column purification (RNeasy, Qiagen). Guide RNAs were tested for cleavage activity by in vitro cleavage assay. Each guide RNA was incubated with Cas9 protein (UNC Protein Expression and Purification Core Facility) and PCR-amplified guide RNA target site. The products were run on an agarose gel for analysis of target site cleavage. Based on this assay, the guide RNA selected for genome editing in embryos was Tardbp-g79T (Supplementary Table 7). The donor oligonucleotide for insertion of the K145Q and silent genotyping mutations was Tardbp-K145Q-T (Supplementary Table 7). Two silent mutations were induced to create a unique HinfI restriction enzyme digestion site and permit genotyping by PCR and gel electrophoresis.

C57BL/6J zygotes were microinjected with microinjection buffer (5 mM Tris-HCl pH 7.5, 0.1 mM EDTA) containing 1) 20 ng/ul Cas9 mRNA, 10 ng/ul g79T guide RNA and 50 ng/ul donor oligonucleotide (founder #9) or 2) 20 ng/ul Cas9 mRNA, 400 nM Cas9 protein, 10 ng/ul g79T guide RNA and 50 ng/ul donor oligonucleotide (founders #23, 26, 39, 44, 53). Injected embryos were implanted in recipient pseudopregnant females and resulting pups were screened by PCR and sequencing for the presence of the desired mutant allele. Founder lines were propagated as heterozygotes and regularly sequenced to confirm retention of the K145Q and silent mutations.

We assessed the likelihood of off-target mutations using prediction algorithms to ensure low likelihood of off-target effects. The Benchling MIT off-target score for Tardbp-g79T is 72(161), and the CRISPOR-generated MIT off-target score is 86. CRISPOR also gave a Cutting frequency determination score of 86(162)–(164). Moreover, all of the predicted exonic off-target sites from CRISPOR have 4 mismatches, making them unlikely to be mutated. Sequencing of the founder lines and their progeny did not detect any insertions or deletions within a 550bp region surrounding the *Tardbp* locus.

TDP-43^{K145Q} mouse line genotyping

Each mouse was genotyped prior to any experimental use. DNA was extracted from ear punch or toe clip tissue using the HotSHOT method(165). PCR amplification of the modified *Tardbp* locus was performed with ApexRed master mix (Genesee Scientific 42-138B) and *TDPKQ* F' and *TDPKQ* R' primers (Supplementary Table 7) using the following cycling parameters: 95°C denaturation for 3min; 15 cycles of 95°C for 30sec, 72°C for 30sec then -1°C per cycle, 72°C 60sec; 25 cycles of 95°C for 30sec, 58°C for 30sec, 72°C for 60sec; 72°C extension for 5min. The PCR product was then incubated with HinfI enzyme (New England Biosystems R0155S) in CutSmart buffer (New England Biosystems B7204) for 1hr at 37°C. Digested PCR products were separated on a 2% agarose Tris-acetate-EDTA gel containing SybrSafe stain (Invitrogen S33102) and visualized on an ImageQuant LAS4000 machine.

Mouse Behavior

All testing was performed by experimenters blinded to mouse genotype.

Open field. Exploratory activity in a novel environment was assessed by a one-hour trial in an open field chamber (41 cm x 41 cm x 30 cm) crossed by a grid of photobeams (VersaMax system, AccuScan Instruments). Counts were taken of the number of photobeams broken during the trial in five-minute intervals, with separate measures for locomotor activity (total distance traveled) and vertical rearing movements. Time spent in the center region was used as an index of anxiety-like behavior.

Conditioned fear. Mice were evaluated for conditioned fear using the Near-Infrared image tracking system (MED Associates, Burlington, VT). The procedure had the following phases: training on Day 1, a test for context-dependent learning on Day 2, and a test for cue-dependent learning on Day 3.

Training. On Day 1, mice were placed in the test chambers, contained in sound-attenuating boxes. The mice were allowed to explore the novel chambers for 2 minutes before presentation of a 30-sec tone (80 dB), which co-terminated with a 2-sec scrambled foot shock (0.4 mA). Mice received 2 additional shock-tone pairings, with 80 sec between each pairing, and were removed from the test chambers 80 sec following the third shock.

Context- and cue-dependent learning. On Day 2, mice were placed back into the original conditioning chambers for a test of contextual learning. Levels of freezing (immobility) were determined across a 5-min session. On Day 3, mice were evaluated for associative learning to the auditory cue in another 5-min session. The conditioning chambers were modified using a Plexiglas insert to change the wall and floor surface, and a novel odor (dilute vanilla flavoring) was added to the sound-attenuating box. Mice were placed in the modified chamber and allowed to explore. After 2 min, the acoustic stimulus (an 80 dB tone) was presented for a 3-min period. Levels of freezing before and during the stimulus were obtained by the image tracking system.

Grip strength. Grip strength was evaluated using precision force gauges. Measures were based on paw grasp of a metal grid by a mouse gently pulled by the tail. Digital force meters (Chatillon DFIS-10; Largo, FL) were mounted on an acrylic platform (San Diego Instruments), with two different grids: a left-hand grid for the front paws, and a right-hand grid for all-four paws. Each grid connected to a force transducer, which provided measures of peak force (newtons). Each mouse was given 3 trials, with at least one minute between each trial. Each trial had 2 components: front-paw measures from the left-hand grid, immediately followed by all-four-paw measures from the right-hand grid.

Rotarod. Subjects were tested for motor coordination and motor learning on an accelerating rotarod (Ugo Basile, Stoelting Co., Wood Dale, IL). For the first test, mice were given three trials, with 45 seconds between each trial. Two additional trials were given 48 hours later. Rpm (revolutions per minute) was set at an initial value of 3, with a progressive increase to a maximum of 30 rpm. across five minutes (the maximum trial length). Measures were taken for latency to fall from the top of the rotating barrel.

Morris water maze. The water maze was used to assess spatial and reversal learning, swimming ability, and vision. The water maze consisted of a large circular pool (diameter = 122 cm) partially filled with water (45 cm deep, 24-26o C), located in a room with numerous visual cues. The procedure involved three separate phases: a visible platform test, acquisition in the hidden platform task, and a test for reversal learning (an index of cognitive flexibility).

Visible platform test. Each mouse was given 4 trials per day, across 2 days, to swim to an escape platform cued by a patterned cylinder extending above the surface of the water. For each trial, the mouse was placed in the pool at 1 of 4 possible locations (randomly ordered), and then given 60 sec to find the visible platform. If the mouse found the platform, the trial ended, and the animal was allowed to remain 10 sec on the platform before the next trial began. If the platform was not found, the mouse was placed on the platform for 10 sec, and then given the next trial. Measures were taken of latency to find the platform and swimming speed via an automated tracking system (Noldus Ethovision).

Acquisition and reversal learning in a hidden platform task. Following the visible platform task, mice were tested for their ability to find a submerged, hidden escape platform (diameter = 12 cm). Each mouse was given 4 trials per day, with 1 min per trial, to swim to the hidden platform. The criterion for learning was an average group latency of 15 sec or less to locate the platform. Mice were tested until the group reached criterion, with a maximum of 9 days of testing. When the group reached criterion (on day 5 in the present study), mice were given a 1-min probe trial in the pool with the platform removed. Selective quadrant search was evaluated by measuring the number of crosses over the location where the platform (the target) had been placed during training, versus the corresponding area in the opposite quadrant. Following the acquisition phase, mice were tested for reversal learning, using the same procedure as described above. In this phase, the hidden platform was re-located to the opposite quadrant in the pool. As before, measures were taken of latency to find the platform. On day 5 of testing, the platform was removed from the pool, and the group was given a probe trial to evaluate reversal learning.

Acoustic startle test. This procedure was used to assess auditory function, reactivity to environmental stimuli, and sensorimotor gating. The test was based on the reflexive whole-body flinch, or startle response, that follows exposure to a sudden noise. Measures were taken of startle magnitude and prepulse inhibition, which occurs when a weak prestimulus leads to a reduced startle in response to a subsequent louder noise.

Mice were placed into individual small Plexiglas cylinders within larger, sound-attenuating chambers. Each cylinder was seated upon a piezoelectric transducer, which allowed vibrations to be quantified and displayed on a computer (San Diego Instruments SR-Lab system). The chambers included a ceiling light, fan, and a loudspeaker for the acoustic stimuli. Background sound levels (70 dB) and calibration of the acoustic stimuli were confirmed with a digital sound level meter (San Diego Instruments). Each session began with a 5-min habituation period, followed by 42 trials of 7 different types: no-stimulus (NoS) trials, trials with the acoustic startle stimulus (AS; 40 msec, 120 dB) alone, and trials in which a prepulse stimulus (20 msec; either 74, 78, 82, 86, or 90 dB) occurred 100 msec before the onset of the startle stimulus. Measures were taken of the startle amplitude for each trial across a 65-msec sampling window, and an overall analysis was performed for each subject's data for levels of prepulse inhibition at each prepulse sound level (calculated as 100 - [(response amplitude for prepulse stimulus and startle stimulus together / response amplitude for startle stimulus alone) x 100].

Tissue harvest and preparation

At each end point, mice were anesthetized deeply with isoflurane and euthanized via rapid decapitation. The hippocampus and neocortex were dissected out of the brain on a cold surface using clean surgical tools, placed into cryo-safe nuclease-free microcentrifuge tubes, flash frozen in liquid nitrogen (LN2), and stored at −80C until processing. Frozen tissue was then pulverized in LN2-cooled stainless steel Cryo-Cups using cold stainless-steel pestles and transferred into cold nuclease-free microcentrifuge tubes and immediately stored at −80C until use.

Solubility fractionation, nucleo-cytoplasmic fractionation, and immunoblotting

All steps of protein fractionation were performed on ice unless otherwise indicated. For solubility fractionation, pulverized tissue was suspended in 5μL/mg of ice-cold 1xRIPA buffer (50mM Tris pH 8.0, 150mM NaCl, 1%NP-40, 5mM EDTA, 0.5% sodium deoxycholate, 0.1%SDS) containing a mix of protease, phosphatase, and deacetylase inhibitors [1μg/mL Peptstatin A (Sigma P4265), 1μg/mL Leupeptin (Sigma L2023), 1μg/mL *N*α-Tosyl-L-lysine chloromethyl ketone hydrochloride (TPCK) (Sigma T7254), 1μg/mL Trypsin inhibitor (Sigma T9003), 1μg/mL N-p-Tosyl-L-phenylalanine chloromethyl ketone (TLCK) (Sigma T4376), 0.67μg/mL trichostatin A, 10mM nicotidamide, 1mM phenyline thanosulfyl fluoride, 1mM phenylmethylsulfonyl fluoride]. The solution was homogenized by sonication and centrifuged at 4°C for 45min at 18000xrcf. The supernatant was removed and saved as the RIPA-soluble (“soluble”) protein fraction. The pellet was resuspended in RIPA buffer with inhibitor mixture, sonicated, and centrifuged as described above, and the supernatant discarded. The resulting pellet of RIPA-insoluble material was resuspended in approximately 1μL/μg of Urea buffer (7M urea, 2M Thiourea, 4%CHAPS, 30mM Tris, pH 8.5) with the inhibitor mixture (as above), sonicated to homogenize, and centrifuged at room temperature (RT) for 45min at 21000xrcf. The resulting supernatant of RIPA-insoluble, urea-soluble protein fraction was saved as the “insoluble” protein fraction.

Nuclear and cytoplasmic soluble proteins were isolated using the Thermofisher NE-PER Nuclear and Cytoplasmic Extraction Kit (Thermo Scientific 78835) per the manufacturer’s instructions, with the addition of the protease, phosphatase, and deacetylase inhibitors (as above) to each buffer.

All soluble protein fractions were analyzed by BCA assay (Thermo Scientific 23225) to determine protein concentration. Equal quantities of protein per sample were run onto 4-20% Tris-Glycine SDS-PAGE gels (Biorad 5671095) under reducing conditions and then transferred onto nitrocellulose membranes. Total transferred protein (TTP) was assessed using PonceauS (Research Products International Corp P56200) protein stain on nitrocellulose membranes per manufacturer’s instructions. Membranes were washed three times in TBST, once in TBS, and blocked in 2% nonfat milk in 1xTBS for 1-2 hours at RT. Membranes were incubated with primary antibodies (Supplementary Table 8) diluted in 2% milk overnight at 4°C. The primary antibody solution was removed and membranes washed three times in TBST, once in TBS, and incubated with cross adsorbed HRP-conjugated goat secondary antibodies (Supplementary Table 8) diluted in 2% milk at 1:10000 or 1:2000 for soluble or insoluble protein immunoblots, respectively, for 1-2 hours at RT. Blots were then visualized by chemiluminescent imaging using an ImageQuant LAS4000 machine. Densitometry analysis to quantify western blot images was performed in LI-COR Image Studio Lite (Lincoln, NE, USA).

Mouse brain RNA isolation, RNA sequencing, and data analysis

Mouse brain tissue was isolated, flash frozen, and pulverized as described above. Approximately 20mg of pulverized brain tissue per sample was used to isolate RNA. 1mL of TRIzol (Invitrogen 15596018) was added to each nuclease-free eppendorf tube containing pulverized tissue, and tissues were lysed via trituration with a P1000 pipette tip, followed by trituration with a 21G and then a 25G needle on a 1mL syringe. Samples were centrifuged at 4°C for 5min at 10,000rcf to remove tissue debris. The supernatant was removed and added to a new tube containing 200uL of chloroform, which were mixed by inversion and cooled on ice for 5min. Samples were centrifuged at 4°C for 15min at 10,000rcf, and the upper aqueous phase containing RNA was transferred into a new tube, followed by the addition of 100uL of isopropanol to precipitate RNA and overnight incubation at -20°C. The next day, samples were centrifuged at top speed (18,000rcf) for 20min at 4°C to pellet the RNA. The pellets were washed twice with 1mL of ice-cold 70% molecular biology grade ethanol and then air dried for 15min at RT. The RNA pellets were resuspended in 20uL of nuclease-free water. On-column DNAse digestion and RNA clean-up was then performed using the Qiagen RNeasy mini kit (Qiagen, Inc. 74106) per manufacturer’s instructions, followed by elution in nuclease-free water.

RNA concentration was assessed using Qubit® RNA BR Assay Kit (Q10210) and a Qubit® 3.0 Fluorometer. RNA integrity was assessed using an Agilent 4150 TapeStation system and associated RNA screen tape reagents (Agilent 5067-5576). Only samples with an estimated RNA integrity number (RIN) ≥7.0 were sent to the New York Genome Center (NYGC) for bulk total RNA sequencing. Upon receipt at NYGC, RNA samples were re-evaluated for quantification and integrity, using Ribogreen and Fragment Analyzer 5300, respectively. Total RNA libraries were prepped using Kapa Total library prep with Ribo-Erase, in accordance with manufacturer recommendations. Briefly, 500ng of total RNA was used for ribosomal depletion and fragmentation of total RNA. Depleted RNA underwent first and second strand cDNA synthesis. cDNA was then adenylated, ligated to Illumina sequencing adapters, and amplified by PCR (using 9 cycles). The cDNA libraries were quantified using Fragment Analyzer 5300 (Advanced Analytical) kit FA-NGS-HS (Agilent DNF-474-1000) and Spectramax M2 (Molecular Devices) kit Picogreen (Life Technologies P7589). Libraries were sequenced on an Illumina NovaSeq sequencer, using paired end sequencing (2 x 100 bp cycles) to a depth of >75M read pairs per sample.

Raw reads were then trimmed and filtered of adapter sequencing using cutadapt(166) and filtered such that at least 90% of bases had a quality score of at least 20. Reads were then aligned to the reference mouse genome (mm10, RefSeq gene annotations) using STAR v2.5.2b(167), and transcript abundance was estimated using salmon(168). Differential expression between TDP43-KQ and TDP43-WT cortex and hippocampus was then detected using DESeq2 v1.34.0(169) in R v4.1.0(170), using a design that corrects for both mouse sex and litter effects. These batch effects were also removed from the VST-normalized expression values using limma(171). The correlation between Log2 fold change values between differentially expressed genes in the cortex and hippocampus was determined and Pearson correlation coefficient and two-sided p-value were computed by ggpubr stat_cor(172),(173), and the smoothed linear model was fit using geom_smooth with method="lm".

Differentially expressed genes ($padj < 0.05$) were then separated into 6 groups based on their intersections between the two brain regions using UpSetR v1.4.0(174) and plotted with ComplexUpset(175). Normalized expression values were then centered around the mean of TDP43-WT for each respective brain region and plotted with ComplexHeatmap(176). Gene Ontology enrichments were then assessed using gprofiler2 v0.2.1(177),(178) and summarized using simplifyEnrichment v1.7.2(179). Previously published differentially expressed genes from Hasan et al(92) and Polymenidou et al(93) were retrieved from the respective publications; significant over-enrichments as well as human gene symbol mappings to mouse orthologs were performed using gprofiler2 (g:Orth). Differential splicing analyses were performed on splice junctions extracted from genome-aligned BAM files using regtools and LeafCutter(180), where tests compared TDP43-KQ to TDP43-WT correcting for sex for each brain region. Results were then summarized and visualized using LeafViz(181).

Quantitative RT-PCR

RNA was isolated from mouse brain tissue as described above. cDNA was generated from 500ng of RNA using Applied Biosystems High-capacity RNA-to-cDNA kit (#4387406) per manufacturer's instructions. Quantitative PCR was performed on a QuantStudio 6 Real Time PCR system (with Thermo Fisher Design & Analysis Software version 2.6.0) using PowerUp SYBR Green master mix (Applied Biosystems A25776). The PCR phase consisted of 40 cycles of 15s at 95°C and 1min at 60°C. Forward and reverse primer sequences for *Tardbp*, *Sort-WT, Sort1-total*, *Sort1-ex17b* and the reference genes *β-Actin* and *Pgk1* are listed in Supplementary Table 7. Relative quantification of transcripts was performed using the Pflaff method(182) with both *β*-Actin and *Pgk1* as reference genes. Primers generated for this paper were designed using PrimerBank(183) and synthesized by Integrated DNA Technologies (IDT).

Tissue Collection, Staining, and Immunofluorescence

Mice were transcardially perfused with 1xPBS followed by 4% PFA, and brains were removed and post-fixed for 24 hours in 4% PFA. Brains were cryoprotected in 15% sucrose in 1xPBS for 24hrs followed then 30% sucrose in 1xPBS for 48hrs, and then embedded in Fisher Tissue-Plus OCT compound (4585). Forebrain (~Bregma +1.78 mm), midbrain (~Bregma +0.50 mm), and hippocampal (~Bregma -1.94 mm) 10 mm cryosections were collected onto Superfrost Plus charged slides using a Leica CM1950 cryostat.

Luxol Fast Blue and Cresyl Violet staining. Slides were acclimated to room temperature and rinsed in distilled water. They were then incubated in 70% ethanol for ~60 hours followed by 95% ethanol for 30 minutes. Tissues were stained with 0.1% Luxol Fast Blue Solution overnight at 60°C, rinsed in distilled water, and differentiated as needed by 0.05% Lithium Carbonate followed by 70% ethanol. They were then counterstained with 0.1% Cresyl Echt Violet, rinsed in distilled water, and differentiated again by 95% ethanol. Finally, slides were dehydrated in 100% ethanol, cleared in Xylene, and coverslipped with DPX mountant (Millipore-Sigma 44581).

Immunofluorescence. Slides were acclimated to room temperature and rinsed in distilled water. Heat-induced epitope retrieval was performed at 120°C using pH 6.0 buffer (Epredia, TA-135-HBL). The tissues were then blocked in 10% normal goat serum for 1 hour. Primary antibodies were applied overnight at 4°C: Mouse Anti-NeuN (clone A60) conjugated to Alexa Fluor 555 (Millipore, MAB377A5), and Rabbit Anti-TDP-43 (Cell Signaling, 89789) or Rabbit anti-Iba1 (Wako, 019-19741) and mouse anti-GFAP conjugated to Alexa Fluor 488 (Cell Signaling, 3655) (Supplementary Table 8). After rinsing, secondary antibodies were applied for 2 hours at room temperature: Alexa Fluor 488 Goat Anti-Rabbit IgG (Invitrogen, A32731) or Alexa Fluor 680 Goat anti-Rabbit IgG (Invitrogen 32734). All antibodies were diluted using

Da Vinci Green Diluent (Biocare Medical, PD900L). Finally, slides were coverslipped using Fluorogel II with DAPI (Electron Microscopy Sciences, 17985-50).

Tissue microscopy and Image Analysis

Brain sections stained with Cresyl Violet (CV) and brain sections labelled with Iba1 and GFAP anatibodies were imaged on a Nikon Eclipse Ti2 widefield microscope equipped with a Nikon DS-Fi3 CMOS color camera (for CV imaging) and a pco.edge 4.2Q High QE sCMOS camera (PCO, Kelheim, Germany) using a 20x/0.5 NA Plan Fluor objective and NIS-Elements software (Nikon, Minato City, Tokyo, Japan). Immunofluorescently labeled brain sections were imaged on a Leica SP8X Falcon confocal microscope equipped with hybrid GaAsP detectors using a 40x/1.30 NA Plan Apochromatic (oil) objective and Leica Application Suite X Life Sciences software (Leica, Wetzlar, Germany). Cell counting (density of CV-positive and NeuN-positive cells), as well as TDP-43 fluorescence intensity, TDP-43 localization measurements, GFAP fluorescence intensity and area, and Iba1 fluorescence intensity and area were performed using CellProfiler(159),(160). Prior to quantifying TDP-43 immunofluorescence intensity and prior to confocal image segmentation, immunofluorescent images were denoised using NIS-Elements Batch Denoise.ai under default conditions. Prior to quantifying Iba1 and GFAP fluorescence characteristics, images of the necortex and hippocampus were cropped to exclude fluorescent signal from the corpus callosum. Within CellProfiler, the Cellpose 2.0 plugin(184),(185) was used to perform neuron identification and the subcellular segmentation of nucleus and cytoplasm within neurons. DAPI fluorescence was used to identify nuclei, and NeuN immunoreactivity was used to identify neuronal nuclei and the surrounding soma. Images were pseudocolored and formatted for publication using Fiji ImageJ(186).

Statistical Analysis

Statistical analysis of RNA sequencing data was performed as described above. All other data was analyzed in GraphPad Prism Version 9.4.1 for Windows, GraphPad Software, San Diego, California USA, www.graphpad.com. For data sets with n>10, outliers were identified and removed (if any) using the ROUT method(187) at Q=1%. Details regarding the statistical test performed, sample sizes, and what the data points and error bars represent can be found in the appropriate figure legends. All statistical tests were two-sided. Statistical significance was determined as p<0.05.

Data availability

The TDP-43^{K145Q} mouse line is now available at the Mutant Mouse Resource and Research Center (MMRRC) at University of North Carolina at Chapel Hill, an NIH-funded strain repository, with the following identifiers (RRID:MMRRC_068119-UNC). Raw and processed RNA-seq data have been deposited to the Gene Expression Omnibus (GEO) under accession GSE216294. All data generated in this work are included in the manuscript and the supporting files. Any plasmids or lentiviruses generated in this study are available upon request.

Supplementary statistical information about data presented in main and supplemental figures can be found in the figure's accompanying source data file. Figures 3, 5, and 7 have accompanying source data files. Supplementary figures S5, S6, and S8 have accompanying source data files.

Author contributions

JCN designed, executed, and directed most of the experiments in this study, primary neuron experiments, primary neuron and hiPSC immunofluorescence, microscopy, and image analysis, mouse brain tissue analysis, protein and RNA isolation, immunoblotting, and data analysis. YC assisted with plasmid preparation, mouse breeding and genotyping, and mouse tissue harvest and mouse perfusion. XT constructed plasmids and generated all lentiviruses. BAE assisted with assays of splicing function. ABM and ASB created and maintained human induced pluripotent stem cell clones, including CRISPR-mediated genome modification, and differentiated hiPSC lines into cortical neurons. PW and DA assisted with mouse handling, immunoblotting, and early characterization of the mouse line. Behavioral testing and initial data analysis was conducted by VDN, KMH, and SSM. JAE performed histology and immunofluorescent labeling of mouse brain sections. SN assisted with immunoblotting. JMS performed RNAseq data analysis and figure construction. This study was supervised and guided by TJC.

Acknowledgements

We would like to thank Dale Cowley and the UNC Animal Models Core Facility for their creation of the TDP-43^{K145Q} mouse line and the initial sequencing. We also thank Natallia Riddick and the UNC Mouse Breeding and Colony Management Core for their assistance in animal husbandry and breeding. Confocal and Nikon Ti2 widefield microscopy was performed at the UNC Neuroscience Microscopy Core (RRID:SCR_019060), supported, in part, by funding from the NIH-NINDS Neuroscience Center Support Grant P30 NS045892 and the NIH-NICHD Intellectual and Developmental Disabilities Research Center Support Grant P50 HD103573, and core director Michele Itano assisted in image analysis protocol design. We are grateful for the UNC Histology Research Core for their assistance in tissue processing and staining. RNA sequencing was performed by the New York Genome Center. The research reported in this publication was supported by the National Institute on Aging (grant F30AG072786), the National Institute on Neurologic Disorders and Stroke (grants R01NS105981, P30NS045892, F31NS122242), the National Institute of General Medical Sciences (grants 1T32GM133364-01A1, 5T32GM008719-19), and the Eunice Kennedy Shriver National Institute of Child Health and Human Development (grants U54HD079124; P50HD103573) of the National Institutes of Health. We also received support from the Department of Defense (grant AL180038) and the Muscular Dystrophy Association (grant MDA573414 and NINDS (P30NS045892).

References

1. Neumann M. (2006) **Ubiquitinated TDP-43 in frontotemporal lobar degeneration and amyotrophic lateral sclerosis** *Science* **314:**130–133

2. Neumann M. , Kwong L. K. , Sampathu D. M. , Trojanowski J. Q. , Lee V. M.-Y. (2007) **TDP-43 Proteinopathy in Frontotemporal Lobar Degeneration and Amyotrophic Lateral Sclerosis: Protein Misfolding Diseases Without Amyloidosis** *Arch. Neurol.* **64:**1388–1394

3. Cairns N. J. (2007) **TDP-43 in Familial and Sporadic Frontotemporal Lobar Degeneration with Ubiquitin Inclusions** *Am. J. Pathol.* **171:**227–240

4. Hogan D. B. (2016) **The Prevalence and Incidence of Frontotemporal Dementia: A Systematic Review** *Can. J. Neurol. Sci.* **43:**

5. Burrell J. R. (2016) **The frontotemporal dementia-motor neuron disease continuum** *The Lancet* **388:**919–931

6. Geser F. , Lee V. M.-Y. , Trojanowski J. Q. (2010) **Amyotrophic lateral sclerosis and frontotemporal lobar degeneration: A spectrum of TDP-43 proteinopathies** *Neuropathol. Off. J. Jpn. Soc. Neuropathol.* **30:**103–112

7. Burrell J. R. , Kiernan M. C. , Vucic S. , Hodges J. R. (2011) **Motor Neuron dysfunction in frontotemporal dementia** *Brain* **134:**2582–2594

8. Giordana M. T. (2011) **Dementia and cognitive impairment in amyotrophic lateral sclerosis: A review** *Neurol. Sci.* **32:**9–16

9. Geser F. (2009) **Clinical and pathological continuum of multisystem TDP-43 proteinopathies** *Arch. Neurol.* **66:**180–189

10. Meneses A. (2021) **TDP-43 Pathology in Alzheimer's Disease** *Mol. Neurodegener.* **16:**84

11. Tomé S. O. (2020) **Distinct molecular patterns of TDP-43 pathology in Alzheimer's disease: relationship with clinical phenotypes** *Acta Neuropathol. Commun.* **8:**61

12. Besser L. M. , Teylan M. A. , Nelson P. T. (2020) **Limbic Predominant Age-Related TDP-43 Encephalopathy (LATE): Clinical and Neuropathological Associations** *J. Neuropathol. Exp. Neurol.* **79:**305–313

13. Nelson P. T. (2019) **Limbic-predominant age-related TDP-43 encephalopathy (LATE): consensus working group report** *Brain* **142:**1503–1527

14. Poulopoulos M. , Levy O. A. , Alcalay R. N. (2012) **The neuropathology of genetic Parkinson's disease** *Mov. Disord.* **27:**831–842

15. Nakashima-Yasuda H. (2007) **Co-morbidity of TDP-43 proteinopathy in Lewy body related diseases** *Acta Neuropathol. (Berl.)* **114:**221–229

16. Gao J. , Wang L. , Huntley M. L. , Perry G. , Wang X. (2018) **Pathomechanisms of TDP-43 in neurodegeneration** *J. Neurochem.* **146:**7–20

17. Boer E. M. J. de (2021) **TDP-43 proteinopathies: a new wave of neurodegenerative diseases** *J. Neurol. Neurosurg. Psychiatry* **92:**86–95

18. Budini M. , Buratti E. (2011) **TDP-43 Autoregulation: Implications for Disease** *J. Mol. Neurosci.* **45:**473

19. Ayala Y. M. (2011) **TDP-43 regulates its mRNA levels through a negative feedback loop** *EMBO J.* **30:**277–288

20. Xu Y. F. (2010) **Wild-type human TDP-43 expression causes TDP-43 phosphorylation, mitochondrial aggregation, motor deficits, and early mortality in transgenic mice** *J. Neurosci.* **30:**10851–10859

21. Igaz L. M. (2011) **Dysregulation of the ALS-associated gene TDP-43 leads to neuronal death and degeneration in mice** *J. Clin. Invest.* **121:**726–738

22. Yang C. (2014) **Partial loss of TDP-43 function causes phenotypes of amyotrophic lateral sclerosis** *Proc. Natl. Acad. Sci.* **111:**

23. Kraemer B. C. (2010) **Loss of murine TDP-43 disrupts motor function and plays an essential role in embryogenesis** *Acta Neuropathol. (Berl.)* **119:**409–419

24. Fratta P. (2018) **Mice with endogenous TDP-43 mutations exhibit gain of splicing function and characteristics of amyotrophic lateral sclerosis** *EMBO J.* **37:**

25. White M. A. (2018) **TDP-43 gains function due to perturbed autoregulation in a Tardbp knock-in mouse model of ALS-FTD** *Nat. Neurosci.* **21:**552

26. Huang S.-L. (2020) **A robust TDP-43 knock-in mouse model of ALS** *Acta Neuropathol. Commun.* **8:**3

27. Stribl C. (2014) **Mitochondrial Dysfunction and Decrease in Body Weight of a Transgenic Knock-in Mouse Model for TDP-43 *** *J. Biol. Chem.* **289:**10769–10784

28. Ebstein S. Y. , Yagudayeva I. , Shneider N. A. (2019) **Mutant TDP-43 Causes Early-Stage Dose-Dependent Motor Neuron Degeneration in a TARDBP Knockin Mouse Model of ALS** *Cell Rep.* **26:**364–373

29. Buratti E. , Baralle F. E. (2010) **The multiple roles of TDP-43 in pre-mRNA processing and gene expression regulation** *RNA Biol.* **7:**420–429

30. Tollervey J. R. (2011) **Characterizing the RNA targets and position-dependent splicing regulation by TDP-43** *Nat. Neurosci. 2011 144* **14:**452–458

31. Cohen T. J. , Lee V. M. Y. , Trojanowski J. Q. (2011) **TDP-43 functions and pathogenic mechanisms implicated in TDP-43 proteinopathies** *Trends Mol. Med.* **17:**659–667

32. Doll S. G. (2022) **Recognition of the TDP-43 nuclear localization signal by importin α1/β** *Cell Rep.* **39:**111007

33. Pinarbasi E. S. (2018) **Active nuclear import and passive nuclear export are the primary determinants of TDP-43 localization** *Sci. Rep.* **8:**7083

34. Kuo P.-H. , Chiang C.-H. , Wang Y.-T. , Doudeva L. G. , Yuan H. S. (2014) **The crystal structure of TDP-43 RRM1-DNA complex reveals the specific recognition for UG- and TG-rich nucleic acids** *Nucleic Acids Res.* **42:**4712–4722

35. Lukavsky P. J. (2013) **Molecular basis of UG-rich RNA recognition by the human splicing factor TDP-43** *Nat. Struct. Mol. Biol.* **20:**1443–1449

36. Duan L. (2022) **Nuclear RNA binding regulates TDP-43 nuclear localization and passive nuclear export** *Cell Rep.* **40:**

37. Ayala Y. M. (2008) **Structural determinants of the cellular localization and shuttling of TDP-43** *J. Cell Sci.* **121:**3778–3785

38. Buratti E. , Baralle F. E. (2012) **TDP-43: gumming up neurons through protein–protein and protein–RNA interactions** *Trends Biochem. Sci.* **37:**237–247

39. Budini M. (2012) **Cellular Model of TAR DNA-binding Protein 43 (TDP-43) Aggregation Based on Its C-terminal Gln/Asn-rich Region *** *J. Biol. Chem.* **287:**7512–7525

40. Pesiridis G. S. , Lee V. M.-Y , Trojanowski J. Q. (2009) **Mutations in TDP-43 link glycine-rich domain functions to amyotrophic lateral sclerosis** *Hum. Mol. Genet.* **18:**–162

41. Sreedharan J. (2008) **TDP-43 Mutations in Familial and Sporadic Amyotrophic Lateral Sclerosis** *Science* **319:**1668–72

42. Kawakami I. , Arai T. , Hasegawa M. (2019) **The basis of clinicopathological heterogeneity in TDP-43 proteinopathy** *Acta Neuropathol. (Berl.)* **138:**751–770

43. Neumann M. (2009) **Molecular Neuropathology of TDP-43 Proteinopathies** *Int. J. Mol. Sci.* **10:**232–246

44. Mackenzie I. R. A. & Neumann, M. (2016) **Molecular neuropathology of frontotemporal dementia: insights into disease mechanisms from postmortem studies** *J. Neurochem.* **138:**54–70

45. Cascella R. (2016) **Quantification of the Relative Contributions of Loss-of-function and Gain-of-function Mechanisms in TAR DNA-binding Protein 43 (TDP-43) Proteinopathies *** *J. Biol. Chem.* **291:**19437–19448

46. Diaper D. (2013) **Loss and gain of Drosophila TDP-43 impair synaptic efficacy and motor control leading to age-related neurodegeneration by loss-of-function phenotypes** *Hum Mol Genet* **22:**1539–1557

47. Lee E. B. , Lee V. M.-Y. , Trojanowski J. Q. (2011) **Gains or losses: molecular mechanisms of TDP43-mediated neurodegeneration** *Nat. Rev. Neurosci.* **13:**38–50

48. Vanden Broeck L. , Callaerts P. , Dermaut B. (2014) **TDP-43-mediated neurodegeneration: towards a loss-of-function hypothesis?** *Trends Mol. Med.* **20:**66–71

49. François-Moutal L. (2019) **Structural Insights Into TDP-43 and Effects of Post-translational Modifications** *Front. Mol. Neurosci.* **12:**301

50. Sternburg E. L. , Gruijs da Silva L. A. , Dormann D. (2022) **Post-translational modifications on RNA-binding proteins: accelerators, brakes, or passengers in neurodegeneration?** *Trends Biochem. Sci.* **47:**6–22

51. Buratti E. (2018) **TDP-43 post-translational modifications in health and disease** *Expert Opin. Ther. Targets* **22:**279–293

52. Cohen T. J. (2015) **An acetylation switch controls TDP-43 function and aggregation propensity** *Nat. Commun.* **6:**

53. Wang P. , Wander C. M. , Yuan C. X. , Bereman M. S. , Cohen T. J. (2017) **Acetylation-induced TDP-43 pathology is suppressed by an HSF1-dependent chaperone program** *Nat. Commun.* **8:**1–15

54. Igaz L. M. (2008) **Enrichment of C-Terminal Fragments in TAR DNA-Binding Protein-43 Cytoplasmic Inclusions in Brain but not in Spinal Cord of Frontotemporal Lobar Degeneration and Amyotrophic Lateral Sclerosis** *Am. J. Pathol.* **173:**182–194

55. Chhangani D. , Martín-Peña A. , Rincon-Limas D. E. (2021) **Molecular, functional, and pathological aspects of TDP-43 fragmentation** *iScience* **24:**102459

56. Agrawal S. , Jain M. , Yang W. , Yuan H. S. (2021) **Frontotemporal dementia-linked P112H mutation of TDP-43 induces protein structural change and impairs its RNA binding function** *Protein Sci. Publ. Protein Soc.* **30:**350–365

57. Chen H.-J. (2019) **RRM adjacent TARDBP mutations disrupt RNA binding and enhance TDP-43 proteinopathy** *Brain J. Neurol.* **142:**3753–3770

58. Chiang C.-H. (2016) **Structural analysis of disease-related TDP-43 D169G mutation: linking enhanced stability and caspase cleavage efficiency to protein accumulation** *Sci. Rep.* **6:**21581

59. Dewey C. M. (2011) **TDP-43 Is Directed to Stress Granules by Sorbitol, a Novel Physiological Osmotic and Oxidative Stressor** *Mol. Cell. Biol.* **31:**1098–1108

60. Colombrita C. (2009) **TDP-43 is recruited to stress granules in conditions of oxidative insult** *J. Neurochem.* **111:**1051–1061

61. Gasset-Rosa F. (2019) **Cytoplasmic TDP-43 De-mixing Independent of Stress Granules Drives Inhibition of Nuclear Import, Loss of Nuclear TDP-43, and Cell Death** *Neuron* **102:**339–357

62. Cohen T. J. , Hwang A. W. , Unger T. , Trojanowski J. Q. , Lee V. M. Y. (2012) **Redox signalling directly regulates TDP-43 via cysteine oxidation and disulphide cross-linking** *EMBO J.* **31:**1241–1252

63. Yu H. (2021) **HSP70 chaperones RNA-free TDP-43 into anisotropic intranuclear liquid spherical shells** *Science* **371:**

64. Ash P. E. A. (2010) **Neurotoxic effects of TDP-43 overexpression in C. elegans** *Hum. Mol. Genet.* **19:**3206–3218

65. Yang C. (2022) **Low-level overexpression of wild type TDP-43 causes late-onset, progressive neurodegeneration and paralysis in mice** *PLOS ONE* **17:**

66. Garcia Morato J. (2022) **Sirtuin-1 sensitive lysine-136 acetylation drives phase separation and pathological aggregation of TDP-43** *Nat. Commun.* **13:**1223

67. Mann J. R. , Donnelly C. J. (2021) **RNA modulates physiological and neuropathological protein phase transitions** *Neuron* **109:**2663–2681

68. Schmidt H. B. , Barreau A. , Rohatgi R. (2019) **Phase separation-deficient TDP43 remains functional in splicing** *Nat. Commun.* **10:**

69. Buratti E. , Baralle F. E. (2001) **Characterization and Functional Implications of the RNA Binding Properties of Nuclear Factor TDP-43, a Novel Splicing Regulator ofCFTR Exon 9 *** *J. Biol. Chem.* **276:**36337–36343

70. Carola V. , D’Olimpio F. , Brunamonti E. , Mangia F. , Renzi P. (2002) **Evaluation of the elevated plus-maze and open-field tests for the assessment of anxiety-related behaviour in inbred mice** *Behav. Brain Res.* **134:**49–57

71. Seibenhener M. L. , Wooten M. C. (2015) **Use of the Open Field Maze to Measure Locomotor and Anxiety-like Behavior in Mice** *J. Vis. Exp. JoVE* 52434 https://doi.org/10.3791/52434

72. Gómez-Nieto R. , Hormigo S. , López D. E. (2020) **Prepulse Inhibition of the Auditory Startle Reflex Assessment as a Hallmark of Brainstem Sensorimotor Gating Mechanisms** *Brain Sci.* **10:**639

73. Mena A. (2016) **Reduced Prepulse Inhibition as a Biomarker of Schizophrenia** *Front. Behav. Neurosci.* **10:**

74. Ueki A. , Goto K. , Sato N. , Iso H. , Morita Y. (2006) **Prepulse inhibition of acoustic startle response in mild cognitive impairment and mild dementia of Alzheimer type** *Psychiatry Clin. Neurosci.* **60:**55–62

75. Chen C. , Kim J. J. , Thompson R. F. , Tonegawa S. (1996) **Hippocampal lesions impair contextual fear conditioning in two strains of mice** *Behav. Neurosci.* **110:**1177–1180

76. Curzon P. , Rustay N. R. , Browman K. E. , Buccafusco J. J. (2009) **Cued and Contextual Fear Conditioning for Rodents** *Methods of Behavior Analysis in Neuroscience*

77. Phillips R. G. , LeDoux J. E. (1992) **Differential contribution of amygdala and hippocampus to cued and contextual fear conditioning** *Behav. Neurosci.* **106:**274–285

78. Kim J. J. , Jung M. W. (2006) **Neural circuits and mechanisms involved in Pavlovian fear conditioning: A critical review** *Neurosci. Biobehav. Rev.* **30:**188–202

79. Marschner A. , Kalisch R. , Vervliet B. , Vansteenwegen D. , Büchel C. (2008) **Dissociable Roles for the Hippocampus and the Amygdala in Human Cued versus Context Fear Conditioning** *J. Neurosci.* **28:**9030–9036

80. Sierra-Mercado D. , Padilla-Coreano N. , Quirk G. J. (2011) **Dissociable Roles of Prelimbic and Infralimbic Cortices, Ventral Hippocampus, and Basolateral Amygdala in the Expression and Extinction of Conditioned Fear** *Neuropsychopharmacology* **36:**529–538

81. Vorhees C. V. , Williams M. T. (2006) **Morris water maze: procedures for assessing spatial and related forms of learning and memory** *Nat. Protoc.* **1:**848–858

82. Nicholls R. E. (2008) **Transgenic mice lacking NMDAR-dependent LTD exhibit deficits in behavioral flexibility** *Neuron* **58:**104–117

83. Watson C. , Kirkcaldie M. , Paxinos G. , Watson C. , Kirkcaldie M. , Paxinos G. (2010) **Chapter 11 - Techniques for studying the brain. in** *The Brain* 153–165 https://doi.org/10.1016/B978-0-12-373889-9.50011-5

84. Mishra M. (2007) **Gene expression analysis of frontotemporal lobar degeneration of the motor neuron disease type with ubiquitinated inclusions** *Acta Neuropathol. (Berl.)* **114:**81–94

85. Gitcho M. A. (2009) **TARDBP 3′-UTR variant in autopsy-confirmed frontotemporal lobar degeneration with TDP-43 proteinopathy** *Acta Neuropathol. (Berl.)* **118:**633–645

86. Chen-Plotkin A. S. (2008) **Variations in the progranulin gene affect global gene expression in frontotemporal lobar degeneration** *Hum. Mol. Genet.* **17:**1349–1362

87. Lord S. J. , Velle K. B. , Mullins R. D. , Fritz-Laylin L. K. (2020) **SuperPlots: Communicating reproducibility and variability in cell biology** *J. Cell Biol.* **219:**

88. Neumann M. (2009) **Phosphorylation of S409/410 of TDP-43 is a consistent feature in all sporadic and familial forms of TDP-43 proteinopathies** *Acta Neuropathol. (Berl.)* **117:**137–149

89. Walker A. K. (2015) **Functional recovery in new mouse models of ALS/FTLD after clearance of pathological cytoplasmic TDP-43** *Acta Neuropathol. (Berl.)* **130:**643–660

90. Eck R. J. , Kraemer B. C. , Liachko N. F. (2021) **Regulation of TDP-43 phosphorylation in aging and disease** *GeroScience* **43:**1605–1614

91. Hallegger M. (2021) **TDP-43 condensation properties specify its RNA-binding and regulatory repertoire** *Cell* **184:**4680–4696

92. Hasan R. (2022) **Transcriptomic analysis of frontotemporal lobar degeneration with TDP-43 pathology reveals cellular alterations across multiple brain regions** *Acta Neuropathol. (Berl.)* **143:**383–401

93. Polymenidou M. (2011) **Long pre-mRNA depletion and RNA missplicing contribute to neuronal vulnerability from loss of TDP-43** *Nat. Neurosci. 2011 144* **14:**459–468

94. JP Ling O. P. , Troncoso JC , Wong PC (2015) **TDP-43 repression of nonconserved cryptic exons is compromised in ALS-FTD** *Science* **349:**650–655

95. Arnold E. S. (2013) **ALS-linked TDP-43 mutations produce aberrant RNA splicing and adult-onset motor neuron disease without aggregation or loss of nuclear TDP-43** *Proc. Natl. Acad. Sci. U. S. A.* **110:**

96. Ma X. R. (2022) **TDP-43 represses cryptic exon inclusion in the FTD–ALS gene UNC13A** *Nat. 2022 6037899* **603:**124–130

97. Melamed Z. (2019) **Premature polyadenylation-mediated loss of stathmin-2 is a hallmark of TDP-43-dependent neurodegeneration** *Nat Neurosci* **22:**180–190

98. Prudencio M. (2020) **Truncated stathmin-2 is a marker of TDP-43 pathology in frontotemporal dementia** *J Clin Invest* **130:**6080–6092

99. Humphrey J. , Emmett W. , Fratta P. , Isaacs A. M. , Plagnol V. (2017) **Quantitative analysis of cryptic splicing associated with TDP-43 depletion** *BMC Med. Genomics* **10:**1–17

100. Trabzuni D. (2012) **MAPT expression and splicing is differentially regulated by brain region: relation to genotype and implication for tauopathies** *Hum. Mol. Genet.* **21:**4094–4103

101. Park S. A. , Ahn S. I. , Gallo J. M. (2016) **Tau mis-splicing in the pathogenesis of neurodegenerative disorders** *BMB Rep.* **49:**405

102. Giesert F. (2013) **Expression Analysis of Lrrk1, Lrrk2 and Lrrk2 Splice Variants in Mice** *PLOS ONE* **8:**

103. La Cognata V. , D’Agata V. , Cavalcanti F. , Cavallaro S. (2015) **Splicing: is there an alternative contribution to Parkinson’s disease?** *neurogenetics* **16:**245–263

104. Rosas I. (2020) **Role for ATXN1, ATXN2, and HTT intermediate repeats in frontotemporal dementia and Alzheimer’s disease** *Neurobiol. Aging* **87:**139

105. Manek R. , Nelson T. , Tseng E. , Rodriguez-Lebron E. (2020) **5'UTR-mediated regulation of Ataxin-1 expression** *Neurobiol. Dis.* **134:**104564

106. Banfi S. (1994) **Identification and characterization of the gene causing type 1 spinocerebellar ataxia** *Nat. Genet.* **7:**513–520

107. Carlo A.-S. , Nykjaer A , Willnow T. E. (2014) **Sorting receptor sortilin—a culprit in cardiovascular and neurological diseases** *J. Mol. Med.* **92:**905–911

108. Hu F. (2010) **Sortilin-Mediated Endocytosis Determines Levels of the Frontotemporal Dementia Protein, Progranulin** *Neuron* **68:**654–667

109. Xu S.-Y. (2019) **Regional and Cellular Mapping of Sortilin Immunoreactivity in Adult Human Brain** *Front. Neuroanat.* **13:**

110. Pallesen L. T. , Vaegter C. B. (2012) **Sortilin and SorLA Regulate Neuronal Sorting of Trophic and Dementia-Linked Proteins** *Mol. Neurobiol.* **45:**379–387

111. Mohagheghi F. (2016) **TDP-43 functions within a network of hnRNP proteins to inhibit the production of a truncated human SORT1 receptor** *Hum. Mol. Genet.* **25:**534–545

112. Tann J. Y. , Wong L.-W. , Sajikumar S. , Ibáñez C. F. (2019) **Abnormal TDP-43 function impairs activity-dependent BDNF secretion, synaptic plasticity, and cognitive behavior through altered Sortilin splicing** *EMBO J.* **38:**

113. Prudencio M. (2012) **Misregulation of human sortilin splicing leads to the generation of a nonfunctional progranulin receptor** *Proc Natl Acad Sci USA* **109:**21510–21515

114. Greiner T. , Kipp M. (2021) **What Guides Peripheral Immune Cells into the Central Nervous System?** *Cells* **10:**2041

115. Prinz M. , Priller J. (2017) **The role of peripheral immune cells in the CNS in steady state and disease** *Nat. Neurosci.* **20:**136–144

116. Scheld M. (2016) **Neurodegeneration Triggers Peripheral Immune Cell Recruitment into the Forebrain** *J. Neurosci.* **36:**1410–1415

117. Pandey S. (2022) **Disease-associated oligodendrocyte responses across neurodegenerative diseases** *Cell Rep.* **40:**111189

118. Neumann M. (2007) **TDP-43-Positive White Matter Pathology in Frontotemporal Lobar Degeneration With Ubiquitin-Positive Inclusions** *J. Neuropathol. Exp. Neurol.* **66:**177–183

119. Mann J. R. (2019) **RNA Binding Antagonizes Neurotoxic Phase Transitions of TDP-43** *Neuron* **102:**321–338

120. Grese Z. R. (2021) **Specific RNA interactions promote TDP-43 multivalent phase separation and maintain liquid properties** *EMBO Rep.* **22:**

121. Berning B. A. , Walker A. K. (2019) **The Pathobiology of TDP-43 C-Terminal Fragments in ALS and FTLD** *Front. Neurosci.* **13:**

122. Wu L. S. (2019) **Transcriptomopathies of pre- and post-symptomatic frontotemporal dementia-like mice with TDP-43 depletion in forebrain neurons** *Acta Neuropathol. Commun.* **7:**50

123. LaClair K. D. (2016) **Depletion of TDP-43 decreases fibril and plaque β-amyloid and exacerbates neurodegeneration in an Alzheimer's mouse model** *Acta Neuropathol. (Berl.)* **132:**859–873

124. Ni J. (2021) **Loss of TDP-43 function underlies hippocampal and cortical synaptic deficits in TDP-43 proteinopathies** *Mol. Psychiatry* https://doi.org/10.1038/s41380-021-01346-0

125. Iguchi Y. (2013) **Loss of TDP-43 causes age-dependent progressive motor neuron degeneration** *Brain* **136:**1371–1382

126. Halliday G. (2012) **Mechanisms of disease in frontotemporal lobar degeneration: gain of function versus loss of function effects** *Acta Neuropathol. (Berl.)* **124:**373–382

127. Gerrits E. (2022) **Neurovascular dysfunction in GRN-associated frontotemporal dementia identified by single-nucleus RNA sequencing of human cerebral cortex** *Nat. Neurosci.* **25:**1034–1048

128. Baker M. (2006) **Mutations in progranulin cause tau-negative frontotemporal dementia linked to chromosome 17** *Nature* **442:**916–919

129. Sieben A. (2012) **The genetics and neuropathology of frontotemporal lobar degeneration** *Acta Neuropathol. (Berl.)* **124:**353–372

130. Greaves C. V. , Rohrer J. D. (2019) **An update on genetic frontotemporal dementia** *J. Neurol.* **266:**2075–2086

131. Sheen V. L. (2004) **Mutations in ARFGEF2 implicate vesicle trafficking in neural progenitor proliferation and migration in the human cerebral cortex** *Nat. Genet.* **36:**69–76

132. Sekiguchi M. (2020) **ARHGAP10, which encodes Rho GTPase-activating protein 10, is a novel gene for schizophrenia risk** *Transl. Psychiatry* **10:**1–15

133. Cuttler K. , Hassan M. , Carr J. , Cloete R. , Bardien S. (1970) **Emerging evidence implicating a role for neurexins in neurodegenerative and neuropsychiatric disorders** *Open Biol.* **11:**210091

134. Duan Y. (2014) **Semaphorin 5A inhibits synaptogenesis in early postnatal- and adult-born hippocampal dentate granule cells** *eLife* **3:**

135. Jung J. S. (2019) **Semaphorin-5B Controls Spiral Ganglion Neuron Branch Refinement during Development** *J. Neurosci.* **39:**6425–6438

136. O'Connor T. P. (2009) **Semaphorin 5B mediates synapse elimination in hippocampal neurons** *Neural Develop.* **4:**18

137. Kantor D. B. (2004) **Semaphorin 5A Is a Bifunctional Axon Guidance Cue Regulated by Heparan and Chondroitin Sulfate Proteoglycans** *Neuron* **44:**961–975

138. Telese F. (2015) **LRP8-Reelin-regulated Neuronal (LRN) Enhancer Signature Underlying Learning and Memory Formation** *Neuron* **86:**696–710

139. Beffert U. (2005) **Modulation of Synaptic Plasticity and Memory by Reelin Involves Differential Splicing of the Lipoprotein Receptor Apoer2** *Neuron* **47:**567–579

140. Reddy S. S. , Connor T. E. , Weeber E. J. , Rebeck W. (2011) **Similarities and differences in structure, expression, and functions of VLDLR and ApoER2** *Mol. Neurodegener.* **6:**30

141. Hinrich A. J. (2016) **Therapeutic correction of ApoER2 splicing in Alzheimer's disease mice using antisense oligonucleotides** *EMBO Mol. Med.* **8:**328–345

142. Hardingham N. , Dachtler J. , Fox K. (2013) **The role of nitric oxide in pre-synaptic plasticity and homeostasis** *Front. Cell. Neurosci.* **7:**

143. Calabrese V. (2007) **Nitric oxide in the central nervous system: neuroprotection versus neurotoxicity** *Nat. Rev. Neurosci.* **8:**766–775

144. Sun L. (2020) **Attenuation of epigenetic regulator SMARCA4 and ERK-ETS signaling suppresses aging-related dopaminergic degeneration** *Aging Cell* **19:**

145. Zhu X. (2001) **Activation of MKK6, an upstream activator of p38, in Alzheimer's disease** *J. Neurochem.* **79:**311–318

146. Alam J. , Scheper W. (2016) **Targeting neuronal MAPK14/p38α activity to modulate autophagy in the Alzheimer disease brain** *Autophagy* **12:**2516–2520

147. Waragai M. (2017) **Importance of adiponectin activity in the pathogenesis of Alzheimer's disease** *Ann. Clin. Transl. Neurol.* **4:**591–600

148. Shi F. (2021) **Comparative Analysis of Multiple Neurodegenerative Diseases Based on Advanced Epigenetic Aging Brain** *Front. Genet.* **12:**

149. Guix F. X. , Uribesalgo I. , Coma M. , Muñoz F. J. (2005) **The physiology and pathophysiology of nitric oxide in the brain** *Prog. Neurobiol.* **76:**126–152

150. Chong C.-M. (2018) **Roles of Nitric Oxide Synthase Isoforms in Neurogenesis** *Mol. Neurobiol.* **55:**2645–2652

151. Seto M. (2022) **Exploring common genetic contributors to neuroprotection from amyloid pathology** *Brain Commun.* **4:**

152. Lou E. (2012) **Tunneling nanotubes provide a unique conduit for intercellular transfer of cellular contents in human malignant pleural mesothelioma** *PloS One* **7:**

153. Schmidt H. B. , Barreau A. , Rohatgi R. (2019) **Decoding and recoding phase behavior of TDP43 reveals that phase separation is not required for splicing function** 548339 https://doi.org/10.1101/548339

154. Beltran A. A. (2021) **Generation of an induced pluripotent stem cell line (UNCCi002-A) from a healthy donor using a non-integration system to study Cerebral Cavernous Malformation (CCM)** *Stem Cell Res.* **54:**102421

155. Battaglia R. A. (2019) **Site-specific phosphorylation and caspase cleavage of GFAP are new markers of Alexander disease severity** *eLife* **8:**

156. C B. (2011) **Reference Maps of human ES and iPS cell variation enable high-throughput characterization of pluripotent cell lines** *Cell* **144:**

157. Chambers S. M. (2009) **Highly efficient neural conversion of human ES and iPS cells by dual inhibition of SMAD signaling** *Nat. Biotechnol.* **27:**275–280

158. Shi Y. , Kirwan P. , Livesey F. J. (2012) **Directed differentiation of human pluripotent stem cells to cerebral cortex neurons and neural networks** *Nat. Protoc.* **7:**1836–1846

159. Carpenter A. E. (2006) **CellProfiler: image analysis software for identifying and quantifying cell phenotypes** *Genome Biol.* **7:**

160. Stirling D. R. (2021) **CellProfiler 4: improvements in speed, utility and usability** *BMC Bioinformatics* **22:**433

161. Anderson K. R. (2018) **CRISPR off-target analysis in genetically engineered rats and mice** *Nat. Methods* **15:**512–514

162. Concordet J.-P. , Haeussler M. (2018) **CRISPOR: intuitive guide selection for CRISPR/Cas9 genome editing experiments and screens** *Nucleic Acids Res.* **46:**

163. Haeussler M. (2016) **Evaluation of off-target and on-target scoring algorithms and integration into the guide RNA selection tool CRISPOR** *Genome Biol.* **17:**148

164. Doench J. G. (2016) **Optimized sgRNA design to maximize activity and minimize off-target effects of CRISPR-Cas9** *Nat. Biotechnol.* **34:**184–191

165. Truett G. E. (2000) **Preparation of PCR-quality mouse genomic DNA with hot sodium hydroxide and tris (HotSHOT)** *BioTechniques* **29:**52–54

166. Martin M. (2011) **Cutadapt removes adapter sequences from high-throughput sequencing reads** *EMBnet.journal* **17:**10–12

167. Dobin A. (2013) **STAR: ultrafast universal RNA-seq aligner** *Bioinformatics* **29:**15–21

168. Patro R. , Duggal G. , Love M. I. , Irizarry R. A. , Kingsford C. (2017) **Salmon provides fast and bias-aware quantification of transcript expression** *Nat. Methods* **14:**417–419

169. Love M. I. , Huber W. , Anders S. (2014) **Moderated estimation of fold change and dispersion for RNA-seq data with DESeq2** *Genome Biol.* **15:**550

170. R Core Team (2022) **R Core Team. R: A Language and Environment for Statistical Computing. (2022).** *R: A Language and Environment for Statistical Computing*

171. Ritchie M. E. (2015) **limma powers differential expression analyses for RNA-sequencing and microarray studies** *Nucleic Acids Res.* **43:**

172. Kassambara A. (2020) **Kassambara, A.ggpubr: 'ggplot2' Based Publication Ready Plots. (2020).** *ggpubr: 'ggplot2' Based Publication Ready Plots*

173. Wickham H. (2016) **ggplot2: Elegant Graphics for Data Analysis**

174. Conway J. R. , Lex A. , Gehlenborg N. (2017) **UpSetR: an R package for the visualization of intersecting sets and their properties** *Bioinformatics* **33:**2938–2940

175. Krassowski M. , Arts M. , Lagger C. (2021) **Krassowski, M., Arts, M. & Lagger, C.krassowski/complex-upset: v1.3.3. (2021) 10.5281/zenodo.5762625.** *krassowski/complex-upset: v1.3.3.*
https://doi.org/10.5281/zenodo.5762625

176. Gu Z. , Eils R. , Schlesner M. (2016) **Complex heatmaps reveal patterns and correlations in multidimensional genomic data** *Bioinforma. Oxf. Engl.* **32:**2847–2849

177. Raudvere U. (2019) **g:Profiler: a web server for functional enrichment analysis and conversions of gene lists (2019 update)** *Nucleic Acids Res.* **47:**

178. Kolberg L. , Raudvere U. , Kuzmin I. , Vilo J. , Peterson H. (2020) **gprofiler2 -- an R package for gene list functional enrichment analysis and namespace conversion toolset g:Profiler**
https://doi.org/10.12688/f1000research.24956.2

179. Gu Z. , Hübschmann D. (2022) **Simplify enrichment: A bioconductor package for clustering and visualizing functional enrichment results** *Genomics Proteomics Bioinformatics*
https://doi.org/10.1016/j.gpb.2022.04.008

180. Li Y. I. (2017) **Annotation-free quantification of RNA splicing using LeafCutter** *Nat. Genet. 2017 501* **50:**151–158

181. Knowles D. A. (2022) **leafviz: A standalone version of the Leafcutter Shiny App**

182. Pfaffl M. W. (2001) **A new mathematical model for relative quantification in real-time RT–PCR** *Nucleic Acids Res.* **29:**

183. Wang X. , Spandidos A. , Wang H. , Seed B. (2012) **PrimerBank: a PCR primer database for quantitative gene expression analysis, 2012 update** *Nucleic Acids Res.* **40:**

184. Stringer C. , Pachitariu M. (2022) **Cellpose 2.0: how to train your own model** https://doi.org/10.1101/2022.04.01.486764

185. Stringer C. , Wang T. , Michaelos M. , Pachitariu M. (2021) **Cellpose: a generalist algorithm for cellular segmentation** *Nat. Methods* **18:**100–106

186. Schindelin J. (2012) **Fiji: an open-source platform for biological-image analysis** *Nat. Methods* **9:**676–682

187. Motulsky H. J. , Brown R. E. (2006) **Detecting outliers when fitting data with nonlinear regression – a new method based on robust nonlinear regression and the false discovery rate** *BMC Bioinformatics* **7:**123

Author information

Julie Necarsulmer
University of North Carolina at Chapel Hill
ORCID iD: 0000-0002-0669-2023

Jeremy Simon
UNC Chapel Hill
ORCID iD: 0000-0003-3906-1663

Baggio Evangelista
University of North Carolina at Chapel Hill

Youjun Chen
University of North Carolina at Chapel Hill

Xu Tian
University of North Carolina at Chapel Hill

Sara Nafees
University of North Carolina at Chapel Hill

Ariana Marquez Gonzalez
University of North Carolina at Chapel Hill
ORCID iD: 0000-0002-0398-1794

Ping Wang
University of North Carolina

Deepa Ajit
University of North Carolina at Chapel Hill

Viktoriya Nikolova
University of North Carolina at Chapel Hill

Kathryn Harper
University of North Carolina at Chapel Hill
ORCID iD: 0000-0002-6297-0032

Jennifer Ezzell
University of North Carolina at Chapel Hill

Adriana Beltran
University of North Carolina at Chapel Hill

Sheryl Moy
University of North Carolina

Todd Cohen
University of North Carolina at Chapel Hill

For correspondence:

toddcohen@neurology.unc.edu
ORCID iD: 0000-0002-4099-0278

Editors

Reviewing Editor
Suzanne Pfeffer
Stanford University, United States of America

Senior Editor
Suzanne Pfeffer
Stanford University, United States of America

Reviewer #1 (Public Review):

With this work, the authors address a central question regarding the potential consequences of post-translational modifications for the pathogenesis of neurodegenerative diseases. Phosphorylation and mislocalization of the RNA binding protein TDP43 are characteristic of ~50% of frontotemporal lobar degeneration (FTLD), as well as >95% of amyotrophic lateral sclerosis (ALS). To determine if acetylation is a primary, disease-driving event, they generated a TDP-43 mutant harboring an acetylation-mimicking mutation (K145Q). Animals carrying the acetylation-mimic mutation (K145Q) displayed key pathological features of disease, including more cytoplasmic TDP43 and impaired TDP43 splicing activity, together with behavioral phenotypes reminiscent of FTLD.

This is a well-written and well-illustrated manuscript, with clear and convincing findings. The observations are significant and emphasize the importance of post-translational modifications to TDP-43 function and disease phenotypes. In addition, the TDP43(K145Q) mice may prove to be a valuable model for studying TDP-43-related mechanisms of neurodegeneration and therapeutic strategies.

However, as it stands it is challenging to determine if any or all of the phenotypes are a direct consequence of interrupted RNA binding by TDP-43, rather than acetylation per se. Furthermore, all the results are obtained using an acetylation-mimic mutation that may simply be disrupting a key residue involved in RNA binding by TDP43, instead of mirroring acetylation itself, which in theory is a reversible modification. Lastly, it remains unknown why TDP43(K145Q) mice developed features of FTLD, but not ALS, despite the fact that TDP-43 acetylation was found in ALS tissue and not FTLD.

Reviewer #2 (Public Review):

This paper extends prior work demonstrating the importance of K145 acetylation of TDP-43 as a post-translational modification that impacts its RNA-binding capacity and may contribute to pathology in FTLD-ALS. The main strengths of this paper are the generation of a novel mouse model, using CRISPR gene editing, in which an acetylation-mimetic mutation (K to Q) is introduced at position 145. Behavioral, biochemical, and genetic analyses indicate that these mice display phenotypes relevant to TDP-43-associated disease and will be a valuable contribution to the field. While most of the data are rigorous and clearly presented, several weaknesses should be addressed to strengthen the manuscript and further characterize the phenotype of mutant mice.

Reviewer #3 (Public Review):

Numerous experimental models are phenotyped in this manuscript including mouse neurons, iPSC-derived human neurons, knock-in mice, and knock-in iPSCs. Expression of acetylation-mimic or acetylation-null TDP-43 protein is achieved either with overexpression or CRISPR-Cas9-based knock-in. A complex phenotype is observed including loss of TDP-43 function (reduced autoregulation, increased cryptic splicing) and a gain of TDP-43 (increased insoluble TDP-43 protein). These correlate with downstream neurobehavioral changes which are most consistent with a cortical/hippocampal phenotype without a motor phenotype. Post-translational modifications of disease-associated proteins are thought to contribute to neurodegenerative disease pathogenesis, and this study succeeds in demonstrating that TDP-43 acetylation results in downstream molecular and behavioral phenotypes.

There are numerous additional strengths. TDP-43 acetylation is a post-translational modification that is known to be associated with TDP-43 inclusions that are characteristic of human diseases. An important strength is the rigorous use of multiple different experimental models (rodent cells, iPSC-derived neurons, mice, overexpression, knock-in) with overall consistent results. Moreover, multiple orthogonal endpoints are presented including histology/cytology/immunostaining, biochemistry, molecular biology, and neurobehavioral assays. As TDP-43 acetylation is known to block RNA binding, these novel cellular and mouse models represent interesting albeit complex tools to study the functional consequences of a partial loss of function. As TDP-43 regulates its own expression (i.e. autoregulation), the complexity lies at least in part due to the loss of RNA binding leading to a functional loss of TDP-43 function which includes the increased expression of the TARDBP transcript and TDP-43 protein.

Conceptually, there is a disconnect in that the mouse model exhibits primarily a cortical/hippocampal phenotype more akin to frontotemporal lobar degeneration with TDP-

43 inclusions (FTLD-TDP), while TDP-43 acetylation is only seen in ALS tissues and not in FTLD-TDP tissues because most of the pathologic protein in the latter is N-terminally truncated (i.e. the acetylation site is not present). That being said, there is no mouse model which completely and faithfully recapitulates the human disease, and this mouse model avoids overt overexpression (increased TDP-43 protein expression stemming from altered autoregulation) and avoids the use of synthetic/artificial mutation (such as mutation of the TDP-43 nuclear localization signal).

In terms of the CNS phenotype, it is difficult to interpret the reduced density of NeuN-positive neurons in the mouse model as a neurodegenerative phenotype. The reduction in NeuN density but not overall cellular density is only suggestive of neurodegeneration (as opposed to, for example, a developmental phenotype) without more rigorous stereological approaches that take into account potential volumetric changes. Indeed, the absence of astrocytosis and microgliosis argues against neurodegeneration.

Some of the loss of function measures (CFTR construct splicing, shift in SORT1 protein) are subtle, although RNA sequencing clearly shows many splicing aberrations including cryptic splicing events which overall supports that a loss of TDP-43 function is observed.

Finally, there are multiple instances where multiple measurements are made on a few biological replicates. ANOVA or t-tests are not appropriate in these instances (lack of independence).